9-7-2023

Structure-from-Motion Derived Snow Cover in Burned Forests of the Western Oregon Cascades

Siobhan Ciafone
Portland State University

Recommended Citation
Ciafone, Siobhan, "Structure-from-Motion Derived Snow Cover in Burned Forests of the Western Oregon Cascades" (2023). *Dissertations and Theses.* Paper 6536.
https://doi.org/10.15760/etd.3671

Structure-from-Motion Derived Snow Cover in Burned Forests of the Western Oregon Cascades

by

Siobhan Ciafone

A thesis submitted in partial fulfillment of the
requirements for the degree of

Master of Science
in
Environmental Science and Management

Thesis Committee:
Kelly Gleason, Chair
Adam Booth
Johnny Ryan

Portland State University
2023

Abstract

Forest fire occurrence in the western US has increased rapidly since the 1980s, and most western US fires occur in the seasonal snow zone. Burned forests influence snow accumulation and melt patterns for years following fire, and understanding drivers of variability in snow cover across a burned landscape at the basin-scale is necessary for accurate hazard prediction and water resource forecasting. Basin-scale surveys of snowpack are possible with remote sensing, but accurate sensing methods such as Light Detection and Ranging (LiDAR) are often cost-prohibitive. In the last decade, structure-from-motion (SfM), an optical remote sensing technique, has emerged as an affordable alternative to LiDAR for high resolution snow depth mapping. While SfM technique has been used to survey snow in unforested regions, this method is not suitable in forested regions due to the inability of RGB cameras to penetrate the forest canopy. Yet the reduced canopy cover of burned forests may offer a unique opportunity to employ this method in regions otherwise not suitable for SfM surveys prior to burn occurrence. To understand the potential and limitations of SfM-derived snow depth and extent maps in burned forests, we collected aerial stereopair imagery over a 27 km^2 region of the burned Breitenbush Watershed in the Oregon Cascades in September of 2022 and February of 2023. We surveyed a smaller region that overlaps the initial survey region in April of 2023. With SfM techniques, we created digital elevation models (DEMs) for each survey. The September DEM was subtracted from February and April DEMs to isolate February and April snowpack.

Coincident with the April survey, 200 depth measurements were taken across five 0.8 km transects along a burn severity gradient. We compared modeled snow depth to measured snow depth at point locations through simple regression to understand how variability in modeled snow was driven by actual snow, and this regression was used to adjust SfM snow depth estimates. We used multilinear regressions to assess how variability in adjusted modeled snow was driven by burn severity, pre-fire vegetation, and topography. We then compared binary snow extent maps to Landsat fSCA through confusion matrices to assess how well SfM snow maps predicted snow extent. Lastly, we limited snow depth maps to an ideal region -high or moderate severity burned forest and snow-covered- and assessed how variability in modeled snow constrained by these conditions was driven by burn severity, topography, and vegetation. Multilinear regression showed that in the sampling region, variability in modeled snow was driven by only burn severity. We observed striking differences in the way terrain was modeled in low severity burn versus moderate and high severity burn. SfM modeled snow in low severity burn was significantly different from modeled snow in moderate and high severity burn. Modeled snow variability was far greater in low severity burn than in high and moderate severity burn, and modeled snow was greater in moderate and high severity burn. Our work indicates that SfM snow modeling in high and moderate severity burn regions is distinct from and likely more reliable than snow modeling in low severity burn regions where canopy cover obscures snow from the sensor.

Acknowledgements

First and foremost, I would like to thank my advisor, Dr. Kelly Gleason, for her support and encouragement throughout this innovative project. I would also like to thank my other committee members, Dr. Adam Booth and Dr. Johnny Ryan, both of whom aided in my understanding of structure-from-motion techniques. Dr. Yangdong Pan was on my committee until the scheduling of my defense, at what point schedule conflicts between committee members could not be resolved, and I appreciate his early support and participation in my proposal defense.

Dr. Johnny Ryan and Devlin Rutherford were instrumental in accurately surveying GCPs and provided equipment for geodetic surveying. 1st Lt. Johnathan Ritchie of the Civil Air Patrol was exceedingly helpful and communicative regarding flight coordination with the WaldoAir. Dr. Brandon Overstreet of the USGS Oregon Water Science Center provided critical troubleshooting support that greatly contributed to my understanding of *Metashape* and my workflow. I extend a huge "thank you" to all these people. Thank you to my lab mates- Anton Surunis, Megan Guinn, Monica Zapata Villegas, and Sage Ebel- who supported my project and learning with their unique skillsets while providing camaraderie that was one of the most satisfying aspects of graduate school.

Lastly, I am grateful for the funding support from the US Army Corps of Engineers, Research and Development Center, contract # W912HZ2220004, as well as support from the USACE Portland Office for Civil Air Patrol flight costs.

Table of Contents

List of Tables

List of Figures

Introduction

1.1 Snow

1.1.1 Importance of Snow

Snow is an essential component of global hydrology, energy, and nutrient cycling. New snow reflects 90% of incoming solar radiation where snow-free vegetation reflects only 15%. As snow may cover up to 50% of the Northern Hemisphere seasonally, the cooling capacity of snow is critical to climate regulation (DeWalle and Rango 2008; Sturm et al. 2017). Forest productivity is driven by both the volume and timing of meltwater, and up to 40% of forests globally exist in seasonal snow zones (Winchell et al. 2016; Barnhart et al. 2016). As forests are critical carbon sink, snow is essential to carbon sequestration (Winchell et al. 2016).

Over one-sixth of the global population relies on run-off generated from the melt from glaciers and seasonal snow, leading some to draw comparisons between mountain snowpack and water towers (Barnett et al. 2005; Viviroli et al. 2007; Li et al. 2017). With storage capacity greater than that of man-made reservoirs, snow-water storage is essential for water resources and ecosystem health in the western US. Snow holds water in cold months and slowly releases water as temperatures warm, bridging a gap between the arrival and demand of precipitation. Thirty-seven percent of precipitation in the western US falls as snow, while fifty percent of total runoff

originates from snow (Li et al. 2017). Of the three largest reservoirs in the western US- Lake Mead, Lake Powell, and Fort Peck Lake- 70% of stored water comes from snow (Li et al. 2017).

1.1.2 Snow and Climate Change in the Western US

Snow water equivalent (SWE) is the amount of liquid water held in snowpack. Peak SWE, the maximum SWE in the snow season and a metric used to assess seasonal snowpack volume, is both decreasing and occurring earlier in the year in response to warming temperatures (Clow 2010; Mote et al. 2005; Musselman et al. 2021; Mote et al. 2018). Since 1950, peak SWE has declined 33% in the western US and ~12% in western North America (Mote et al. 2018; Musselman et al. 2021). April 1 has historically marked the transition from accumulation to ablation (melt) in the snow season, yet 34 - 42% of Snow Telemetry (SNOTEL) stations indicate a rise in accumulation-season melt, blurring the distinction between accumulation and melt seasons (Musselman et al. 2021). Knowles et al. (2006) observed the ratio of snowy days to all days with precipitation decrease at 87% of sites observed in the western US. While less snow accumulates and snowpack disappears faster, warmer temperatures are driving shifts from snow to rain.

Snowmelt onset and snow disappearance are similarly advancing across the West (Harpold et al. 2014; Clow 2010). Over a 30-year period beginning in the late 1970s, Clow (2010) observed snow melt onset across Colorado SNOTEL stations advance 1.9 - 7.5 days per decade while the day of the centroid of snowpack advanced 1.1 - 5.6 days per decade. Earlier

melt onset may advance days of melt into winter when solar radiative forcing is minimal compared to melt days in spring or summer (Musselman et al. 2017). Musselman et al. (2017) suggest that in a warming climate scenario, 64% of snow cover that would otherwise exhibit high to moderate melt rates will exhibit slow melt rates. High melt rates limit the amount of time that meltwater is partitioned between streamflow and evapotranspiration. In this way, rapid melt brings soil to field capacity, a necessary condition for groundwater recharge and overland flow (Barnhart et al. 2016). Conversely, slower snowmelt promotes the loss of meltwater to the atmosphere and suppresses groundwater recharge. Warmer temperatures also increase atmospheric demand for moisture, compounding effects of warming on the partitioning of melt between streamflow and evapotranspiration (Knowles et al. 2018).

As streamflow generation is driven by snowmelt, earlier snowmelt results in earlier streamflow generation in snow-dominated basins (Stewart et al. 2004). Of 279 snow-dominated rivers in the western US observed from 1948 - 2000 by Stewart et al. (2004), the center of mass flow shifted 10-30 days for most observed streams. Earlier snowmelt precedes solar radiation optimal for vegetation growth, negatively impacting forest productivity and peak biomass (Steltzer et al. 2009). Early season depletion of the snowpack unsurprisingly diminishes late season forest productivity, leading to late season drought (Knowles et al. 2018; Trujillo et al. 2012).

1.1.3 Snow and Climate Change in the Pacific Northwest

Increases in temperature over the latter half of the 20th century drove declines in peak SWE of up to 40% in the Cascade Range of the Pacific Northwest, which are the greatest declines in SWE in the entire western US (Mote et al. 2018). Snow in the PNW is characterized as maritime, meaning that peak SWE is high, the accumulation season is short, and that snow melts early and quickly compared to continental snowpack (Trujillo and Molotch 2014). PNW snow accumulates at near-freezing temperatures and low altitudes compared to continental snowpack, such that less warming is required to melt snow and for precipitation to fall as rain, leading some to describe PNW snow as "at risk" (Nolin & Daly 2006; Mote 2003). As mean annual temperatures are higher and elevations lower in the PNW than the Intermountain West, impacts of climate change on snowpack are exacerbated in the PNW (Mote 2003; Trujillo and Molotch 2014; Mote et al. 2018; Nolin and Daly 2006).

Rain-on-snow (ROS) events, a phenomenon that increases downstream flood risk, rapidly depletes snowpack, and is expected to increase in response to warming temperatures in high elevation snowpack, are frequent in the PNW compared to other regions (Musselman et al. 2018; McCabe et al. 2007). With a pseudo-global warming climate simulation, Musselman et al. (2018) estimate basin runoff volumes due to ROS events to increase more than 100% in the Cascade range. Similarly, shifts in days of snowfall to rainfall and advances timing of streamflow generation are most pronounced in the Pacific Northwest (Knowles et al. 2006; Stewart et al. 2004).

1.1.4 Snow and Fire in the Western US

Forest fire occurrence and extent in the western US increased abruptly in the 1980s, when forest fire frequency increased four times that of previous decades and burned area increased 650% (Westerling et al. 2006). Within the same period, the fire season (time between first fire reposted and last fire controlled) increased by 78 days (Westerling et al. 2006). The occurrence of large forest fires is highly inversely correlated with early snow disappearance, with 56% of fires and 72% of burned areas occurring in early snowmelt years (Westerling et al. 2006). From 2000-2012, more than 80% of fires in the western US burned in the seasonal snow zone and these fires were 4.4 times larger than those outside of the snow zone (Gleason et al. 2013). In the western US, burn area and forest fire frequency is increasing most rapidly in the Pacific Northwest (Westerling et al. 2006).

Early snowmelt is strongly associated with spring temperature and earlier snow disappearance, both of which drive forest fire occurrence (Westerling et al. 2006). Warm temperatures and earlier snow disappearance cause the growing season to begin earlier in the year, resulting in increased drought likelihood and greater fire risk as snowmelt contributions to ground and surface water are depleted earlier in the summer (Gleason et al. 2019). Diminished post-fire forest canopy may reduce interception of snow, potentially promoting greater snow accumulation, while simultaneously promoting increased total solar radiation. Burned forests shed black carbon and burned woody debris (BWD) onto snow, decreasing snow albedo and increasing radiative forcing on snow (Gleason et al. 2013). Forest fire may impact snow albedo

for up to 15 years following fire (Gleason et al. 2019). In 2013, Gleason et al. found that despite greater snow accumulation in a forest the year following fire, snow albedo decreased by 40% in the ablation season. This same study found that snow disappeared 23 days earlier and melted twice as fast as snow in nearby unburned forest (Gleason et al. 2013). Given the importance of snow for downstream water resources, understanding the impact of fire on snow at the watershed is important for water forecasting.

1.1.5 Structure-from-Motion Remote Sensing to Detect Snow

Given changes in snow accumulation and ablation patterns and increased ROS risk beneath a changing climate, estimating snowpack metrics to quantify snowpack volume and patterns of accumulation and melt are of interest to water managers and scientists. Remote sensing allows researchers to go beyond interpolation of point-data measurements of snow and is necessary to understand spatiotemporal trends in snow accumulation and melt. Remote sensing also allows researchers to survey regions otherwise inaccessible or hazardous for *in situ* measurements, typical characteristics of mountainous, snowy regions.

The most accurate methods for collecting data with high spatiotemporal resolution and minimal uncertainty, such as drone-based LiDAR (Light Detection and Ranging), are cost prohibitive and the equipment cumbersome (Westoby et al. 2012; Bühler et al. 2015). The spatial range of drone-based LiDAR is constrained such that basin-scale surveys are not possible in a single survey. While optical remote sensing of snow is widespread (eg. Landsat fSCA,

MODIS snow-cover products), products detail either snow extent or SWE at spatial resolutions too coarse to capture variability in snowpack across a basin (Bühler et al. 2015).

In recent years, structure-from-motion photogrammetry (SfM) has emerged as a low-cost system for topographic reconstruction. SfM derives 3D models from 2D imagery through matching identifiable features across overlapping, offset images (explained in greater detail below). While photogrammetry was experimentally applied to snowpack modeling as early as the 1960s, advances in photogrammetric software, consumer grade cameras, GPS devices, and computer processing capabilities have situated photogrammetry at the forefront of snowpack remote sensing only in the last decade (Nolan et al. 2015; Westoby et al. 2012).

The proliferation of studies that have used SfM to map snow depth in the last decade is illustrated in Table 1 (all papers listed examine the success of SfM methodology with various equipment across diverse land types and scales). SfM has been used to map snow with centimeter accuracy at sub-kilometer scales and decimeter accuracy at kilometer scales using both unmanned aerial systems (UAS) and airplanes, the two primary methods of image capture for SfM workflows. While UAVs allow for lower flying altitude and higher resolution maps, SfM sensors mounted on airplanes are capable of surveys at watershed scales (Meyer et al. 2022). Worldview and Pléiades satellites have also been used for stereo-photogrammetry reconstruction of snow, but this imagery is most effective over flat, homogeneous terrain. Successful SfM surveys have typically been executed in non-forested regions or with vegetated areas masked.

Table 1. Current work using SfM to map snow depth across various spatial scales.

Author	Aircraft, flying altitude	Survey Area	Resolution	Accuracy	Topography and vegetation	Georeference of snow-on
Adams et al. 2018	Fixed-wing UAS, 400 m above ground level	.12 km^2	.5 m	4 - 33 cm	Mixed, boulders <5 meters, clustered trees 1-3 meters, mean slope 6 °. Vegetated areas set to 0 in snow map.	GNSS/IMU and 7 GCPs, co-registration of snow-free region
Bühler et al. 2015)	Airplane, 1500 m above ground	26.25km^2 , 119 km^2	2 m	30 cm	Mountainous, all vegetation above 1.5 meters is masked	GNSS/IMU and 11-33 GCPs
Bühler et al. 2016	Fixed-wing UAS	.057 - .363 km^2	10 cm	7 - 30 cm	Valley (1) with mixed vegetation, mountain top (mean 30° slope, max 90°) (2)	GNSS/IMU. Natural, snow-free reference points used
Meyer and Skiles 2019	Airplane, 1555 m AGL	3.2 km^2	1 m	14 cm	Senator Beck Basin, vegetation masked	GNSS/IMU. Snow-free areas used to co-register with LiDAR.
Meyer et al. 2022	Airplane, above ground altitude not provided	300 km^2	3 m (DTM) & 50 m (SWE)	NMAD of 0.19 m	mountainous (1,420 m relief). Grassland, mixed conifer, alpine meadow.	GNSS/IMU. Snow-free areas used to co-register with LiDAR.
Nolan et al. 2015	Airplane, above ground altitude not provided	5- 35 km^2 (3 study areas)	6 - 10 cm	Centimeter - decimeter	Airport (1), mixed tundra with sparse vegetation (2), river valley (3)	Multi-frequency GPS (10cm accuracy), GCPs only used for co-registration
Walker et	fixed-wing	0.75 to	1 m	15 cm	Shrub-tundra	GNSS/IMU,

al. 2021	UAS, 100 m	2.35 (total 9.6) km^2	(1-2 m shrubs),	50 GCPs

1.1.6 Structure-from-Motion to Detect Snow in Burned Forests

As with all optical remote sensing of snow, SfM is limited in forested regions as forest canopy obscures the snow below. While this effect may be more navigable with LiDAR data as the return of ground signal may be filtered from canopy returns, SfM is a passive technique that utilizes only the visible spectrum. As such, many researchers elect to survey a non-forested area (eg. above tree line), mask forests from SfM surveys of snow, or set forested areas to 0 in digital elevation models (DEM) of difference (Bühler et al. 2015; Meyer and Skiles 2019; Adams 2016). Meyer et al. (2022) evaluated variability in SfM accuracy and mapped a 300 km^2 watershed with coincident LiDAR and SfM (Table 1). The greatest negative error values produced by SfM were found in vegetation-classified pixels (-4 m to -28 m). Similarly, Nolan et al. (2015) found that even with image resolution of 15 centimeters, the influence of trees on DEMs could not be fully resolved and resulted in the greatest snow depth estimation error (though map overall accuracy was still 10 cm).

While it is known that SfM is not effective when ground is obscured by vegetation, the degree to which SfM may be useful (albeit less accurate) in sparsely forested regions is not well understood. Howland et al. (2022) make the case for employing SfM in sparsely vegetated regions to bypass the cost of LiDAR data collection. By classifying and interpolating between ground points, Howland et al. (2022) estimate a digital terrain model with SfM in a forested

region. It is possible that this technique could be used to map snow in forests, provided gaps in trees allow a view of the snow.

1.2 Structure-from-Motion Workflow

1.2.1 Key Point Detection, Correspondence, and Filtering

The first step in the SfM workflow is to detect points visible across multiple images that can be used for image matching. These points, called 'key points', are invariant to changes in scale and rotation and partially invariant to orientation and illumination (Westoby et al. 2012). Key points are distinct because of the intensity of their pixels compared to surrounding pixels. The Scale Invariant Feature Transform (SIFT) object recognition system is commonly used to identify key points. Images are incrementally blurred with a Gaussian Blur and subtracted from one another. Differenced images are stacked and extrema identifiable across all magnitudes of blur are selected as key points. Comparing points across varying magnitudes of Gaussian Blur ensures that key points are effective across camera viewpoints and resolution.

After key points are identified, a 'descriptor' is assigned to each point. A descriptor is a series of vectors that describe intensity image gradients originating from key points and acts as a key point signature. As key point identification relies on intensity gradients, high resolution gradients with high contrast produce the most key points (Westoby et al. 2012). Following key-point identification, descriptors are compared across images. Descriptors are matched across images using nearest-neighbor algorithms, and tracks are drawn between key points (Figure 2).

Key points that were stationary on the camera lens were discarded, as this indicated an object on the sensor (ie., a scratch, dirt, or a part of the plane visible to the sensor).

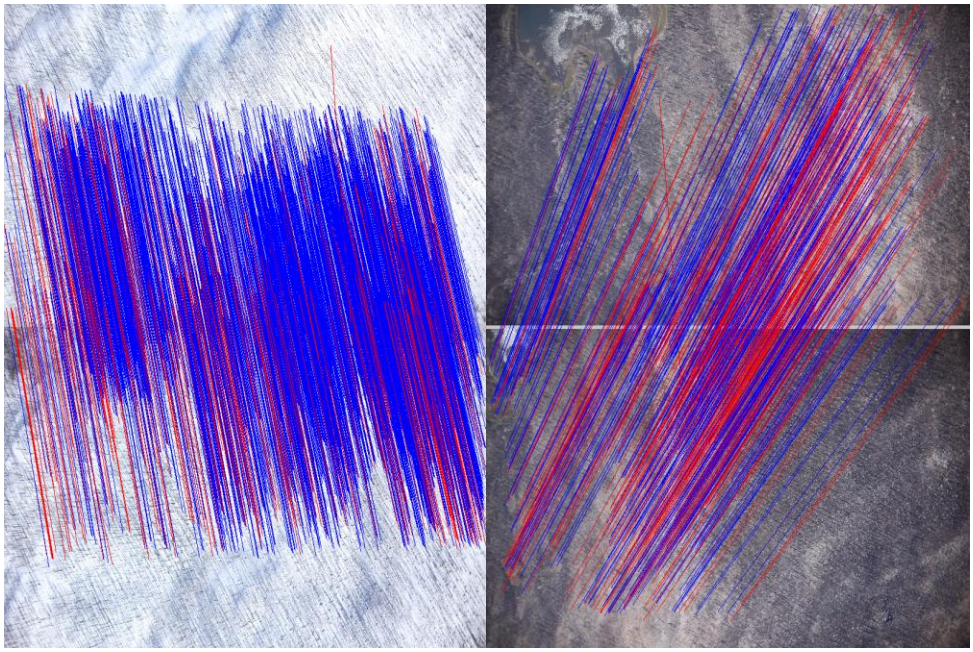

Figure 1. Examples of tracks used to match key points between images. The left photos show a snow-on flight, the right photos show images from the bare-earth flight. Blue lines indicate accepted tracks; red lines indicate discarded tracks.

1.2.2 Structure-from-Motion with Bundle Adjustment

SfM is defined by the process of simultaneously estimating 3D structure, camera location and orientation, and camera calibration parameters (camera focal length, coordinates of the image principal point), and lens distortion coefficients from key points (*Agisoft Metashape User Manual*; Carrivick et al. 2016). This process is widely referred to as Bundle Adjustment. According to Carrivick et al. (2016), "bundle adjustment produces jointly optimal 3D structure and viewing parameter", where "jointly optimal" refers to model estimates that limit error in both camera position and environment structure. Bundle adjustment works on a

pair of images with the greatest number of successful tracks and incrementally introduces images of fewer tracks to the model. The aim of the model is to minimize reprojection error, which is the difference between the estimated 3D position of a point and the points' position on an image. Once a model with minimal reprojection error has been determined, triangulation between key points is used to create a sparse cloud of estimated 3D structure. Where a 'key point' is a feature easily identifiable in multiple images (2D) that may be used to estimate image positionality and overlap, a 'tie point' is a 3-dimensional point estimated from key point triangulation.

Multi-view stereo (MVS) techniques are applied to SfM sparse clouds to create a dense cloud that can be used for DEM generation and difference detection, leading many to call 3D scene construction from overlapping imagery SfM-MVS. MVS point cloud density is greater than that of the sparse cloud by at least two orders of magnitude (Carrivick et al. 2016). MVS builds upon image matches determined in bundle adjustment. Image matches are grouped via Clustering MVS (CMVS) algorithms and Patch-Based MVS algorithms (PMVS) are used to construct 3D data from image clusters.

1.2.3 Georeferencing with Ground Control Points

An SFM-MVS model is created in imaginary space with an arbitrary coordinate system. To georeference the model, either highly accurate camera coordinates derived from real-time kinematic GPS and an inertial measurement unit or integration of ground control points (GCP)

is necessary (Carrivick et al. 2016). GCPs are natural or installed features on the ground that are visible in imagery and have precisely surveyed latitude, longitude, and elevation. GCPs are identified in photos after bundle adjustment but before dense cloud creation. Surveyed GCP coordinates are paired with arbitrary coordinates and a model transformation applied. The most beneficial GCPs are positioned on flat ground to minimize lateral distortions in imagery and contrast strongly with their surroundings. According to Carrivick et al. (2016), a minimum of 3 GCPs are required to georeference and scale a point cloud. In this study, we use camera coordinates to provide approximate camera locations and GCPs to increase model accuracy.

1.3 Study Objectives and Research Question

In the Oregon Cascades, all but the high peaks are forested, and remote sensing of snow is difficult under the best circumstances. Yet difficult data collection coincides with the greatest increases in fire, losses of SWE due to climate warming, and increases in ROS hazards in the West, making monitoring snowpack in the Oregon Cascades paramount. With the proliferation of forest fire in the seasonal snow zone of Oregon and the accessibility and spatiotemporal capacity of airborne SfM, we assess the accuracy at which SfM can detect snow in burned forests of the Oregon Cascades at the basin scale, a scale useful for water resource managers. **Ultimately, we address the following questions: (1) how is variability in basin-scale SfM derived snow maps driven by forest density, topography, and burn severity, and (2) can SfM detect trends in snow depth in stand-replacing fire where canopy is eliminated?**

We address these questions by comparing *in situ* snow depth measurements to modeled snow depth derived from coincident aerial SfM surveys conducted several times throughout the 2022-2023 snow season. To understand what drives variability in SfM models, SfM snow depth was modeled by forest density, burn severity, and topography. Modeled variables and variable sources are depicted in a conceptual model (Figure 1). We expect to find that (1) variability will be greatest in unburned forests, and (2) variability will be smallest in the high severity burned forests with low vegetation density.

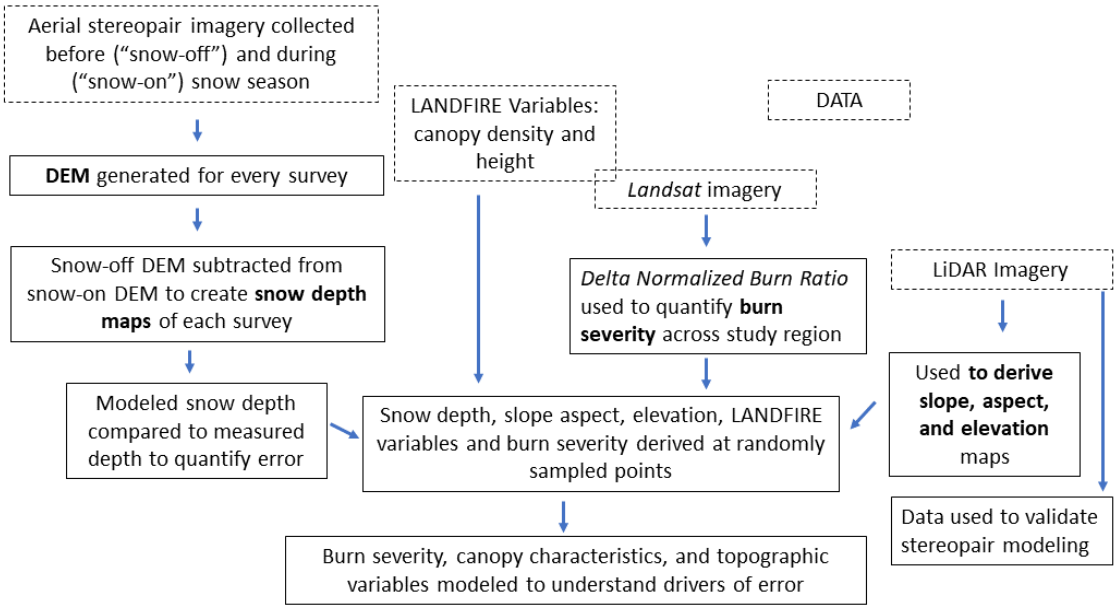

Figure 2. Conceptual model of study. Variables used to explain variability in SfM snow models included.

Methods

2.1 Study area

This analysis was focused on the Brietenbush basin in the Oregon Cascades (Figure 3). The North Fork and South Fork Breitenbush rivers converge into the Breitenbush River, which drains into the Santiam River and supplies water for the city of Salem. In August 2020, 77% of the Brietenbush basin burned in the Lionshead Fire. The Lionshead fire was part of a massive fire complex known as the Labor Day Fires that ultimately burned 1 million acres across the Oregon Cascades, exceeding the area burned in the region over preceding 36 years (Abatzoglou et al. 2021). The Lionshead Fire burned 200,000 acres on the flanks of Mt. Jefferson in the Deschutes and Willamette watersheds. The burned region is heavily forested and burned heterogeneously.

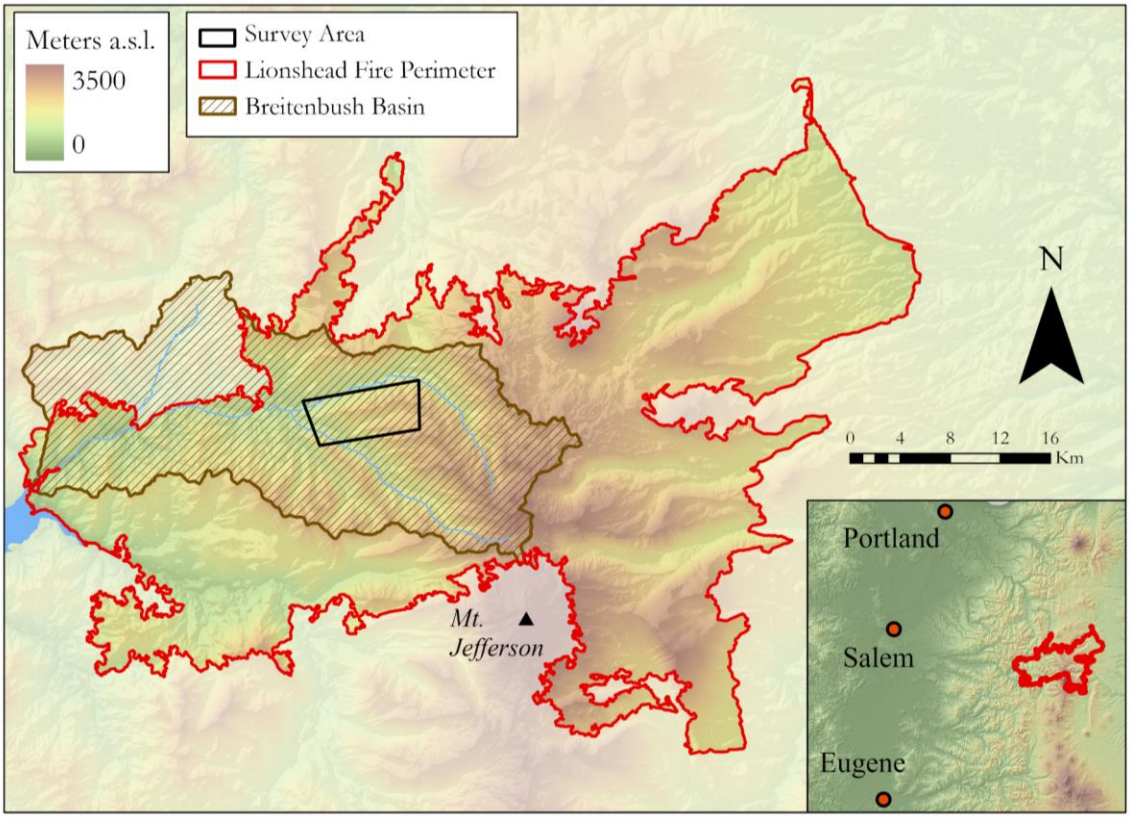

Figure 3. The study region lies within the Breitenbush Basin, 77% of which was burned in Lionshead Fire. Inset shows where the burn scar is located in relation to major cities.

2.2 Survey Region and Flight Paths

2.2.1 2021-2022

While surveys were scheduled for the 2021-2022 snow season, the sensor used in this study was temporarily grounded by the US Air Force in March of 2022 (surveys are conducted by an auxiliary Air Force fleet, the Civil Air Patrol, see section 3.2 for details). A bare-earth flight and single snow-on flight were conducted for this period, but photos were ultimately discarded due to issues with image overlap at high elevations. Between the 2021-2022 and 2022-2023 survey seasons, the survey region was shifted slightly within the drainage to an area with less

complex topography (Figure 4). Data collection used in this study was collected throughout the 2022-2023 snow season.

2.2.2 2023-2023

During the 2022-2023 snow season, a bare-earth flight was conducted in September of 2022, and snow-on surveys were scheduled for the first of each month from February until snow disappearance. While flights were scheduled for the first of each month, weather frequently delayed deployment, often for multiple weeks. Flights ultimately occurred on February 25th and April 28th. While a flight was scheduled for early June, snow melted rapidly in the survey region, so we elected to cancel the final flight.

The survey region was refined, and flight lines were adjusted after the bare-earth and February 25 survey. The initial 27 km^2 survey region was constrained to 16.8 km^2 at the highest elevations of the initial polygon (Figure 4). The densely forested lower elevation regions of the initial polygon were eliminated and the coverage of burned, upper elevation regions (where the most ground is visible,and we expect the model to perform the best) improved. All surveys up to and including the February 25 survey were executed with only parallel flight paths. As the constrained polygon took less time to survey, perpendicular flight lines were added to the survey and the region was imaged twice as much (Figure 5). The survey area contains logged regions, high and mixed severity burn, and forested regions, allowing and model effectiveness to be

compared across land class and for burned regions to be compared to open regions (logged regions).

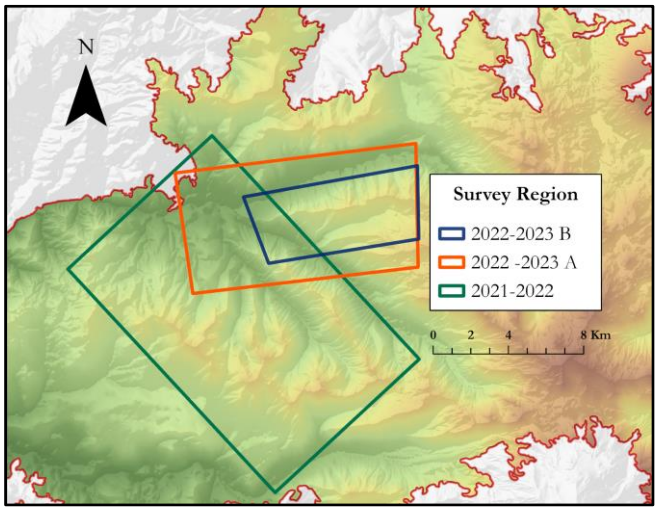

Figure 4. The survey region was adjusted throughout the period of study. A bare-earth flight and single snow-on flight were flown in the 2021-2022 survey region, after which the WaldoAir was grounded for the remainder of the season. The bare-earth flight for the 2022-2023 season was flown in the 2022-2023 A polygon, as was the February 25 flight. The April 2022-2023 flight was flown in the reduced polygon, polygon 2022-2023 B.

The bare-earth and February flights consisted of seven 8-km east-west flight lines with 75% front and side overlap. The April flight included seven 6-km east-west flight lines and five 2.6-km north-south flight lines with 75% front and side. While roll, pitch, and yaw are not corrected for post-processing, abundant overlap corrects for potential distortions (Ritchie, Jonathan 1st Lt, personal communication).

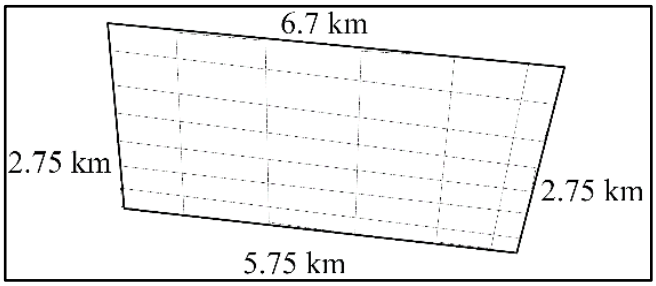

Figure 5. Survey polygon dimensions and interior flight lines for polygon - 2022-2023 B. All other flights (2021-2022 polygon and 2022-2023 A) were flown with only E-W flight lines.

Table 2. Survey region and imagery collection specifications for each survey.

	September 2022	**February 25 2023**	**April 28 2023**
Flight Region Area	27 km^2	27 km^2	16.8 km^2
Flight Pattern	Parallel	Parallel	Parallel and perpendicular
Flight Orientation	E-W	E-W	E-W; N-S
Flight altitude (AGL)	1 km	1 km	1 km
Validation	LiDAR	10 depth measurements	200 depth measurements
GSD	10-cm at highest elevation	10-cm at highest elevation	10-cm at highest elevation

2.3 Image Acquisition

Stereopair imagery was collected using a WaldoAir XCAM Ultra50 RGB Sensor mounted on a manned airplane. The WaldoAir pod is equipped with two 50 mm Canon EOS 5DS R lenses. The plane and sensor used for imagery collection are owned and operated by the Civil Air Patrol, a civilian auxiliary fleet of the US Air Force (Figure 6). The pod is equipped with an internal micro-electro-mechanical system (MEMS) inertial measurement unit (IMU) and a Novatel OEMStar GPS to directly georeference photos. The WaldoAir sensor has two cameras offset 20° from each other (10° from nadir) with 40° image angle, allowing for overlap between camera images and 60° viewing angle total. Image dimensions of each camera are 8,688 x 5792 pixels (100 Mp combined). The Waldo Flight Control software is used to plan flightlines over a target polygon with a target overlap percentage. Photo metadata include the latitude,

longitude, and altitude of the sensor at the time of image capture. Shutter speed was set to 1/2000 seconds.

Figure 6. (A) CAP plane, (B) WaldoAir mounted on the plane wing, (C) image of sensor from below showing the two cameras.

2.4 Ground Control Points

Six GCPs were distributed in corners and the center of the study area for the bare-earth survey while GCPs were placed along an elevation gradient for snow-on surveys (Figure 7). GCPs for the snow-off survey were more dispersed than for the snow-on surveys given the greater accessibility of forest roads in summer. Bare-earth GCPs consisted of six 4x4 planks of wood spray painted with a black 'X' (the center of which was surveyed) and secured to the ground with a rebar. In order to easily transport GCPs on skis for snow-on surveys, tarps rather than planks were secured to surveyed t-posts. With the support of University of Oregon colleagues (J. Ryan and D. Rutherford), GCPs were surveyed at 20 cm accuracy with an Emlid Reach GNSS Receiver.

Weather windows suitable for flights in early spring 2023 were infrequent and fleeting. If GCPs were left in the field for only a few days, they could be covered by snow and no longer visible in imagery. Flights were sometimes scheduled less than 12 hours beforehand, necessitating prompt fieldwork deployment for GCP installation and ground truthing. Given these constraints, spring GCPs were typically installed on the morning of scheduled flights. As returning to the field the day after surveys was not reasonable, tarps were left in the field where they were either buried with snow or remained on the snow surface. Snow depth was recorded at the center of GCPs unless preferential melt occurred around tarps from previous surveys, in which case depth measurements were taken at each side of the tarp beyond the visible influence of preferential melt and averaged.

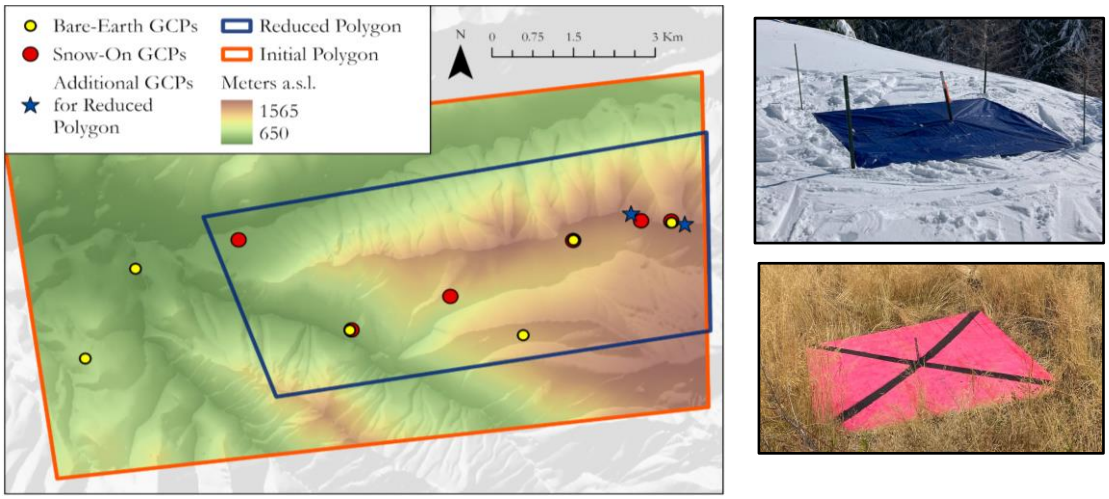

Figure 7. (Left) GCP locations for bare-earth and snow-on flights. After the survey region was reduced, two GCPs were added at high elevations. The additional GCPs were present for the April 28 flight but not for the February flight. (Top-right) Snow-on GCPs were tarps so that they could be easily transported on skis and (bottom-right) bare-earth GCPs were wooden planks. The planks required no additional securements but were transported by car.

Table 3. GCP locations and survey error for snow-on GCPs. GCP 7 and 8 were only included in the April 28 survey.

GCP	Longitude	Latitude	Ellipsoidal Height (m)	Elevation RMS (cm)	Lateral RMS (cm)
1	-121.9538918	44.78118108	-121.9538918	2.575	0.986
2	-121.9538907	44.78118365	-121.9538907	0.763	0.326
3	-121.9188702	44.77409934	-121.9188702	0.601	0.308
4	-121.8986131	44.78110844	-121.8986131	0.008	0.008
5	-121.8873915	44.78354542	-121.8873915	0.081	0.044
6	-121.8824076	44.78352913	-121.8824076	0.023	0.028
7	-121.8886576	44.78447253	-121.8886576	0.008	0.012
8	-121.8801462	44.7831656	1466.839	0.015	0.014

2.5 Model Snow Depth Validation with Snow Depth Measurements

In order to validate and characterize error of modeled snow depth, 200 georeferenced snow depth measurements were taken on April 28th (Figure 8). Due to shorter days and more snow (and therefore longer travel time on skis and more arduous GCP deployment), such robust coincident ground-truthing was not completed for the earlier February 25th survey. Ten snow depth measurements coincident with the February 25th survey served only as validation.

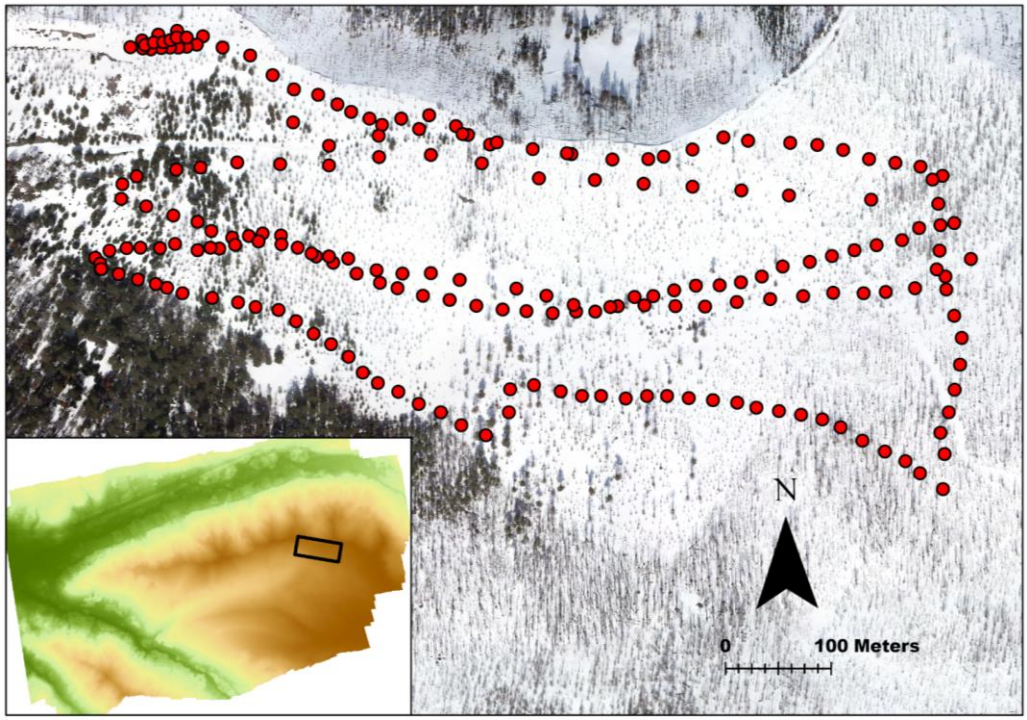

Figure 8. Points of ground-truth measurements and (inset) location of ground-truthing within the survey region.

April 28th snow depth measurements were taken with a Magnaprobe GPS Snow Depth Probe (hereafter GPS probe; SnowHydro 2013). The probe measures snow up to 120 cm depth, which was shallower than some of the snowpack at the time of surveying. When depth measurements exceeded 120 cm, the GPS probe recorded the maximum value- 120 cm- while the correct depth was measured with a 3-meter depth probe. As each GPS probe record has an index in addition to a coordinate and depth measurement, depth measurements could be corrected post-survey by index.

2.6 Processing of SfM Imagery

Stereopair photos from all surveys were processed in *Agisoft Metashape*. *Metashape* processing workflow was primarily adapted from Over et al. (2021). A digital elevation model

of the bare-earth flight was subtracted from a co-registered snow-on DEM to construct snowpack across the study region. The processing workflow for constructing digital terrain models in *Metashape* is detailed in the following sections.

2.6.1 Photo Alignment Through Bundle Adjustment

Photos from the bare-earth and snow-on flight are added to *Metashape*, which automatically separates images into separate groups by camera (either of the two WaldoAir cameras), information which is sourced from image metadata. Once all images are added to the project, images are aligned at high accuracy, meaning that photos are not downscaled for bundle adjustment. The accuracy settings determine the quality at which camera positions are estimated at the expense of processing time. The default key point limit of 60,000 and tie point default limit of 0 were used, where 0 indicates infinite tie points or 'no limit'. The default error of 10 meters was assigned to each image location as the image coordinate error was not known. At this point, images were aligned and a sparse cloud estimated. Images that failed to align (typically 0-5 total) were removed from further processing. After image alignment, ground control points (GCPs) were added to the project. Lateral and vertical accuracy of each GCP was incorporated into the model.

2.6.2 Optimization and Tie-Point Reduction Through Gradual Selection

Prior to dense cloud production, tie points are filtered by estimated error in three steps: reconstruction uncertainty, projection accuracy, and reprojection error. Reconstruction

accuracy concerns uncertainty due to camera geometry, projection accuracy is uncertainty related to key points, and reprojection accuracy is uncertainty between where a point is located on an image and the 3D location it is projected to (Over et al., 2021). As recommended by Over et al. (2021), points are filtered sequentially by reconstruction accuracy, projection accuracy, and lastly reprojection accuracy.

Every time points are deleted, the model is "optimized", meaning that camera parameters and point positions are re-estimated from the reduced sparse cloud. The goal of point reduction is to minimize reconstruction accuracy root mean squared error (RMSE) to less than or equal to 0.3 pixels (Over et al., 2021). Therefore, points are deleted until reconstruction accuracy RMSE is no longer minimized by point reduction. As optimal RMSE may be achieved through filtering by any of the three parameters, this is the most subjective step in photogrammetric processing. It was observed that the parameter that RMSE was most responsive to (reconstruction uncertainty, projection accuracy, or reprojection error) varied by model. Ten percent of points are selected and deleted until RMSE is not depreciated through point selection, deletion, and model optimization by a particular parameter.

2.6.3 Dense Cloud Construction, Point Classification, and DEM Construction

Once points were filtered, they were used to create a dense cloud. Dense cloud 'quality' setting may be set to low, medium, or high, with quality achieved at the expense of processing time. The 'depth filtering' setting ranges from mild to aggressive, with aggressive the

recommended setting for aerial imagery. High quality and aggressive filtering parameters were used to create dense clouds unless aggressive filtering resulted in large gaps in the dense cloud, in which case filtering intensity was iteratively decreased from medium to mild until there were no gaps.

Once the dense cloud was created, ground points were classified. This step is critical when attempting to create a digital terrain model (DTM) in a forested region as high vegetation is classified and removed (if vegetation was included, the map would be a digital surface model). The *Metashape* tool "Classify Ground Points" was used rather than the "Classify Points" tool as the former provides greater parameterization of ground-point selection. With this tool, points are classified as binary "ground" or "not ground", and only ground points are used to create the DTM. When classifying ground points, the *Metashape* user establishes the maximum angle possible between potential ground points, the maximum distance between potential ground points, and the cell size that the dense cloud is divided into prior to ground point sampling. For this study, we set the maximum angle to 30°, maximum distance between points to 10 meters, and the cell size to 50 meters. A DTM is a type of DEM, and maps used in this analysis are referred to as DEMs.

2.6.4 DEM Co-registration, Post-Processing, and DEMs of Difference

Co-registration, which refers to an applied vertical or horizontal shift of a DEM so that it precisely overlaps with a reference DEM, is essential to difference detection even after

georeferencing. Bare-earth imagery was processed with snow-on imagery, automatically co-registering flights at the expense of processing time. Photos from snow-on and bare-earth flights were processed simultaneously in Bundle Adjustment (3.5.1) and gradual selection and optimization steps described above (3.5.2), after which images from each flight were separated into different "chunks" within the *Metashape* project. To use the above 4D workflow for difference detection requires that large regions of the DEMs are unchanged to allow key-point matching across photo sets (Over et al., 2021). This method was used despite the majority change of ground cover between bare-earth and snow-on surveys due to the presence of large regions of no snow in the snow-on imagery, the incorporation of GCPs into the project, and the likelihood of stationary trees to be used as key points. DEMs were exported from *Metashape* at 0.3-meter resolution.

2.7 Statistical Modeling of SfM Modeled Snow

2.7.1 Independent Variables

At all measured snow depth locations, modeled snow depth and variables expected to drive variability in the modeled snow were extracted. All driving variables and their sources and collection year are included in Table 3.

Table 4. Variable sources, variables, and year of product acquisition.

Source	Variables	Year
LANDFIRE	Vegetation cover (%) , height (m), and class (herb, shrub, tree)	2016 (pre-fire)
Monitoring Trends in Burn Severity (MTBS)	Relative difference Normalized Burn Ratio (RdNBR) and classified burn severity	Pre-Fire Image Date: August 10, 2020 (S2B) Post-Fire Image Date: August 10, 2021 (S2A)
Forest Service (LiDAR)	Digital Elevation Model. Derived variables include elevation, aspect, and slope	2020

Burn Metrics: RdNBR and Burn Severity

Variables that quantify forest burn were sourced from Monitoring Trends in Burn Severity (MTBS), a USDA and USGS program. MTBS offers three products that quantify burn at 30-m spatial resolution: delta normalized burn ratio (dNBR), relative dNBR (RdNBR), and thematic burn severity (a classified burn severity product). dNBR is calculated by differencing pre - and post-fire NBR:

$$NBR = (NIR - SWIR)/(NIR + SWIR)$$

Where near infrared (NIR) detects chlorophyll and middle infrared (or short-wave infrared, SWIR) detects moisture in soil and vegetation. A pre-fire image is selected as close to the start of fire as possible while a post-fire image is selected as close to the anniversary of the pre-fire image as possible to control for phenology and solar angle variance. As dNBR quantifies changes in total biomass, dNBR indicates greater burn in densely vegetated areas. This may be problematic if the purpose of using a burn metric is to quantify net changes to a landscape rather than

biomass loss. To account for this, dNBR may be relativized by pre-fire vegetation through the RdNBR equation:

$$RdNBR = dNBR / SquareRoot(ABS(NBR\ pre\text{-}fire / 1000))$$

While vegetation is an important driver of error in SfM and snow depth variability, vegetation variability is captured by LANDFIRE variables (discussed below). To avoid redundancy, RdNBR was used for modeling rather than dNBR. An example of how dNBR and RdNBR values may correspond to on-the-ground burn severity may be seen in Table 5.

In addition to continuous dNBR and rdNBR products, MTBS produces a classified burn severity map. Classes include (1) unburned to low, (2) low, (3) moderate, (4) high, and (5) increased vegetation. While classes are consistent across all fires processed by MTBS, dNBR and thresholds used to distinguish classes are determined for each fire. While continuous RdNBR values exclude the subjectivity introduced through classification, classified burn severity is necessary for pairwise assessment of error by burn. Therefore, both RdNBR and classified burn severity are used in this analysis.

Table 5. Example classification parameters for dNBR and RdNBR as determined by Miller and Thode (2007). Parameters are subjective to individual fires and based on thresholds determined by the analyst.

Class	dNBR	RdNBR
Unchanged	< 41	< 69
Low	41- 176	69 - 315
Moderate	177- 366	316 - 640
High	>=367	>=641

Vegetation Variables: Height, Percent Coverage, and Class

Vegetation maps were sourced from Landscape Fire and Resource Management Planning Tools (LANDFIRE), a USDA and USDOI program. This study uses two LANDFIRE products that characterize vegetation at 30-m spatial resolution: Existing Vegetation Cover (EVC) and Existing Vegetation Height (EVH). Pixels are classified as either tree, shrub, or herb (this is consistent between EVC and EVH), and EVC characterizes each pixel by percent coverage of each class while EVH characterizes each pixel by height of each class (eg., pixel EVH may be "Shrub = 0.8 m" and EVC may be "Shrub = 30%"). In this way, EVH and EVC are categorical variables. To achieve a continuous metric of vegetation cover and height, the pixel class was removed from EVC and EVH metrics and three metrics were created: class, height, and percent cover. As herb and shrub cover were assumed to not affect imagery (as herbs and shrubs were covered by snow), percent cover for herb and shrub pixels was set to 0. A final metric to describe land cover from LANDFIRE was derived by classifying tree pixels as "forested" and shrubs and herbs as "unforested".

Much of the region where ground-truthing occurred was classified as "shrub" or "herb" in the 2022 LANDFIRE dataset, likely due to the diminished canopy cover of burned forest. While these designations accurately indicate that little to no canopy cover in burned forests, trees in these regions are unaccounted for in the EVC dataset yet expected to impact SfM point estimation. The impact of burn on LANDFIRE designation was such that these variables were a better indicator of burn severity rather than forest density. As burn severity is accounted for

in modeling with MTBS variables and as forest density in tandem with burn severity is expected to affect SfM accuracy, a clear metric of forest density unaffected by burn severity is necessary. To achieve this, LANDFIRE variables for 2016 (the most recent pre-fire product) were incorporated into regression models to account for antecedent pre-fire conditions. Another motive for using 2016 LANDFIRE data was that these data captured far greater variability than 2022 classifications (2016 EVC contained 39 unique values where 2022 EVC contained 5; 2016 EVC contained 26 unique values where 2022 EVC contained 5).

Topographic Variables: Elevation, Aspect, and Slope

Topographic variables include elevation, slope, and aspect. A 1-meter resolution LiDAR-derived DEM of the study region was provided by a USGS colleague (B. Overstreet). This was used to produce slope and aspect maps. Aspect was converted from degrees to categorical directions (N, NE, E, SE, S, SW, W, NW).

2.7.2 SfM Snow Depth Modeling with Multilinear Regression

SfM modeled snow depth was found by subtracting the bare-earth DEM from snow-on DEMs to isolate snow. After extracting April SfM modeled snow depth values at *in-situ* measurement coordinates, we found that SfM snow depth values were up to an order of magnitude greater than measured snow depth values. Therefore, a simple linear model with measured snow depth as the driving variable and modeled snow depth as the response was used to correct snow depth maps. Once the April SfM map was corrected, 100 points were randomly

generated within the *in-situ* measurement domain. April SfM modeled snow and driving variables were extracted at all points. Snow depth was then regressed by burn severity, topography, and vegetation variables (Section 3.7.1). As robust coincident ground truthing was only completed for the April survey, this analysis was completed with April data.

Variables that did not correlate significantly with SfM modeled snow (p-value $\leqq 0.05$) were removed to create a minimally adequate model with lowest Akaike information criterion (AIC). The deviance of the full and reduced model was compared through an ANOVA test. If deviance of models was not significantly different, it was assumed that the reduced model was as effective in accounting for the variability as the full model.

The resolution of DEMs output from *Metashape* was 0.3-meters. To understand if variability in the April 0.3-meter resolution SfM snow map impacted results, this map was sampled to 30-meters and the process repeated. After resampling the 0.3-meter DEM to 30-meters, multiple ground-truthed snow depth measurements fell in the same pixel. To avoid over-reporting these snow depth estimates, all duplicated modeled snow depth values were removed from further analysis. The relationship between measured snow and 30-meter resolution modeled snow at measurement locations was similarly established through simple regression, which was then used to correct randomly sampled snow depth values. Once significant drivers of variability in SfM modeled snow were identified, the relationship between drivers and modeled snow were further investigated through univariate analysis.

2.7.3 Snow Extent and Snow Depth Mapping

To assess the accuracy of modeled snow extent, a binary snow extent map was derived from each survey and compared to a Landsat Fractional Snow-Covered Area (fSCA) image captured as close to the survey date as possible. To create a snow extent map, all SfM snow map pixels that were greater than 0 (meters) were classified as 1 and all pixels less than or equal to 0 were classified as 0. The classified snow maps were resampled to 30-meters, the resolution of Landsat imagery. Landsat fSCA bundles contain two fSCA products: Fractional Snow-Covered Area and Canopy Adjusted Fractional Snow-Covered Area. In this instance, we used Canopy Adjusted fSCA as this map better accounts for the influence of forest canopy on snow coverage estimations.

Pixels in Landsat fSCA maps are assigned a value between 0 and 100, where 100 indicates the entire pixel is snow covered and 0 indicates none of the pixel is snow covered. After visually comparing fSCA to survey orthomosaics, we decided to set a threshold for "snow-covered" as fSCA ≥ 75. One thousand points were randomly generated where Landsat fSCA and modeled snow extent maps overlapped. Binary pixel values were extracted from classified rasters at each random point. These values were used to create a confusion matrix with Landsat fSCA as the reference dataset and modeled snow extent as the prediction dataset.

Finally, we created snow depth maps for February and April. February and April snow depth maps were adjusted by regressions between measured and modeled snow discussed in

section 2.7.2. A mask was applied that constrained snow maps to high and moderate severity burn regions. Snow maps were further constrained to snow-covered regions, as determined by Landsat fSCA (fSCA ≥ 75 was considered snow-covered). In this way, we created our most 'ideal' snow depth maps. One thousand points were randomly sampled over snow depth map domains, and SfM snow depth and driving variables were extracted at point coordinates. Modeled snow depth was regressed by vegetation, burn severity, and topography to investigate drivers of variability in SfM snow maps at the basin scale.

Results

3.1 Linear Modeling of Modeled Snow

3.1.1 Modeling of Measured and Modeled Snow

Measured and modeled snow depth were significantly related at 0.3- and 30-meter resolutions (0.3-meter modeled snow depth = 3.2453 (measured depth) + 3.0497; p-value = 1.083×10^{-10}, adjusted R-squared = 0.1844; 30-meter resolution modeled snow = 3.0258 (measured depth) + 3.5621; p-value = $2.582 \times x10^{-8}$, adjusted R-squared = 0.1396) (Figure 9). Yet modeled snow depth values were up to an order of magnitude greater than measured snow depth values. Therefore, the above regressions were used to adjust modeled snow depth. Based on these relationships between measured and modeled snow, the following equations were used to adjust SfM modeled snow depth maps:

1. 0.3-meter adjusted snow depth = 0.059875(0.3-meter modeled snow) + 0.772229
2. 30-meter adjusted snow depth = 0.05866(30-meter modeled snow) + 0.78194

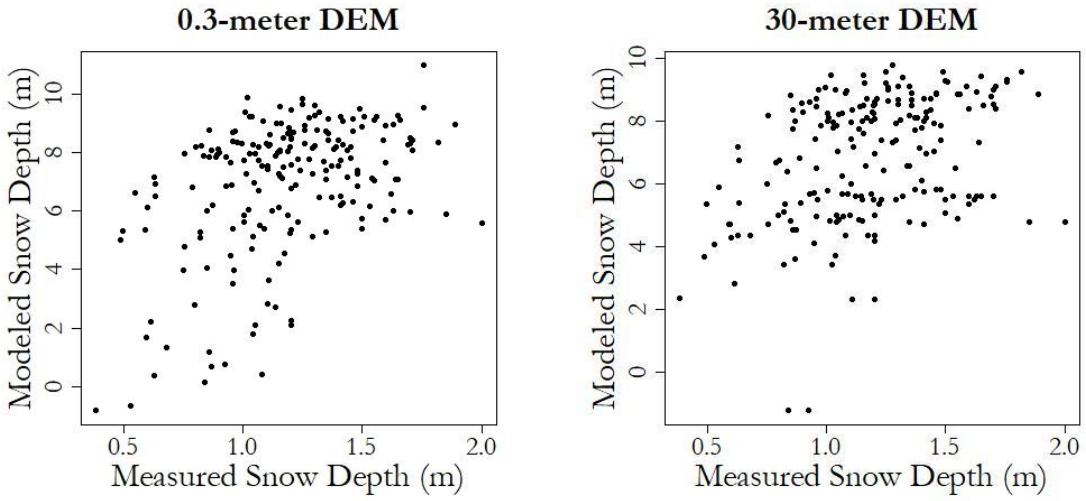

Figure 9. 0.3-meter (left) and 30-meter (right) estimated snow depth (y-axis) plotted against measured depth (x-axis). The relationship between measured and modeled snow was used to correct SfM modeled snow depth valued within the measurement domain.

3.1.2 Drivers of Variability in 0.3-Meter Modeled Snow

An initial regression between 0.3-meter modeled snow and driving variables accounted for 40.55% of variability in modeled snow (adjusted R-squared = 0.4055, p-value =2.766×10^{8}). Of driving variables in the initial model, RdNBR (p-value = 6.01×10^{-5}) was the only significant driver of variability. The minimally adequate model therefore incorporated only RdNBR (0.3-meter modeled snow = 7.7×10^{-4} (RdNBR) - + 0.5; adjusted R-squared = 0.4108; p-value = 4.126×10^{-13}) and performed as well as the complete model (ANOVA F-statistic p-value = 0.5248). Burn severity was positively related to modeled snow, which is expected as high severity burn forests exhibit greater snow accumulation. While we expected burn severity to influence modeled snow, we also hypothesized that vegetation would influence model variability in

tandem with burn severity. Neither vegetation cover nor height were significant predictors of variability.

3.1.3 Drivers of Variability in 30-Meter Modeled Snow

The initial regression between 30-meter resolution modeled snow and driving variables predicted 40% of variability in modeled snow, with RdNBR (p-value = 0.000128), and elevation (p-value = 0.039328) significant driers of variability (adjusted R-squared = 0.4039, p-value = 3.062×10^{-8}). The minimally adequate model also predicted 40% of variability in 30-meter modeled snow, with RdNBR the only significant driver of variability and elevation falling out of the model (30-meter modeled snow = 6.906×10^{-4} (RdNBR) + 0.58; adjusted R-squared = 0.4037, p-value = 7.468×10^{-13}). An ANOVA test was used to determine that the reduced model performed as well as the initial model (ANOVA F-statistic p-value = 0.4508). R-squared values for the 0.3-meter and 30-meter resolution maps were both roughly 0.4, and in both instances the minimally adequate model only included RdNBR as a driving variable. In this way, resolution did not impact the strength of the relationship between SfM modeled snow and driving variables.

3.1.4 Analysis of Variance: Classified Burn Severity

Given that burn severity was the only significant driver of variability in SfM snow maps, we assessed how SfM modeled snow varied by classified burn severity. While the MTBS classified burn severity product has 5 classes (see section 3.7.1), randomly sampled points fell in

pixels classified as low, medium, or high severity with 10, 17, and 73 occurrences, respectively. The following ANOVA tests were completed for the full dataset and for subsampled data, where *n* sample = *n* smallest class. As there were 10 occurrences of sampling in low severity burn, 10 moderate and high severity burn samples were randomly sampled from the full dataset. The following analyses were completed for SfM maps at 0.3-meter resolution.

3.1.5 Classified Burn Severity: SfM Modeled and Measured Snow Depth

Prior to assessing SfM modeled snow variability by burn severity class, we characterized modeled snow depth by burn severity class for the full dataset (high severity mean = 1.2 (meters), standard deviation = 0.1; moderate severity mean = 1.1, standard deviation = 0.2; low severity mean = 0.35, standard deviation = 0.6) and the sampled dataset (high severity mean = 1.3 (meters), standard deviation = 0.1; moderate severity mean = 1.1, standard deviation = 0.2; low severity mean = 0.35, standard deviation = 0.6). When assessing the means and medians of burn severity groups, high and moderate severity burns exhibit the greatest (modeled) snow depth (Figure 10).

An ANOVA of the full dataset indicated that 0.3-meter resolution SfM modeled snow varied by burn severity (ANOVA F-statistic p-value $< 2 \times 10^{-16}$). We used a post-hoc Tukey HSD test to determine that modeled snow in low and high severity groups (p-value = 0.00) and moderate and low severity groups (p-value =0.00) were statistically different while modeled snow in moderate and high severity groups were similar (Figure 10). An ANOVA test of the

sampled dataset similarly showed that modeled snow varied by burn severity (ANOVA F-statistic p-value = 9.68×10^{-6}). Also similar to the full data set, SfM modeled snow in low and high severity burn (p-value = 0.00) and low and moderate burn (p-value = 0.00) were significantly different while modeled snow in moderate and high severity burn was similar (Figure 10).

Full Dataset

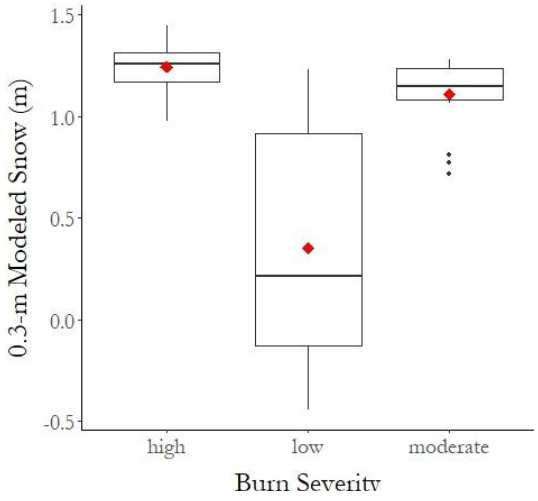

Sampled Data

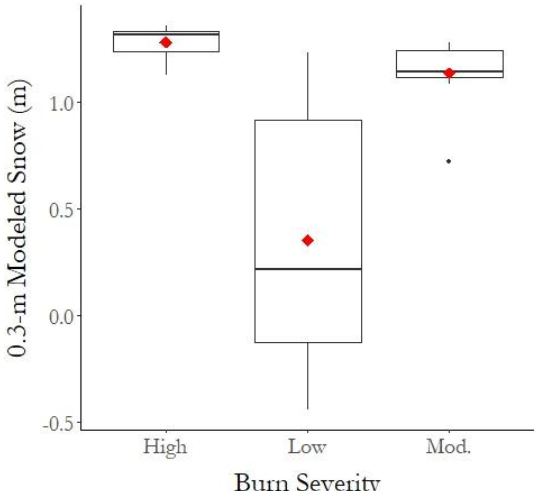

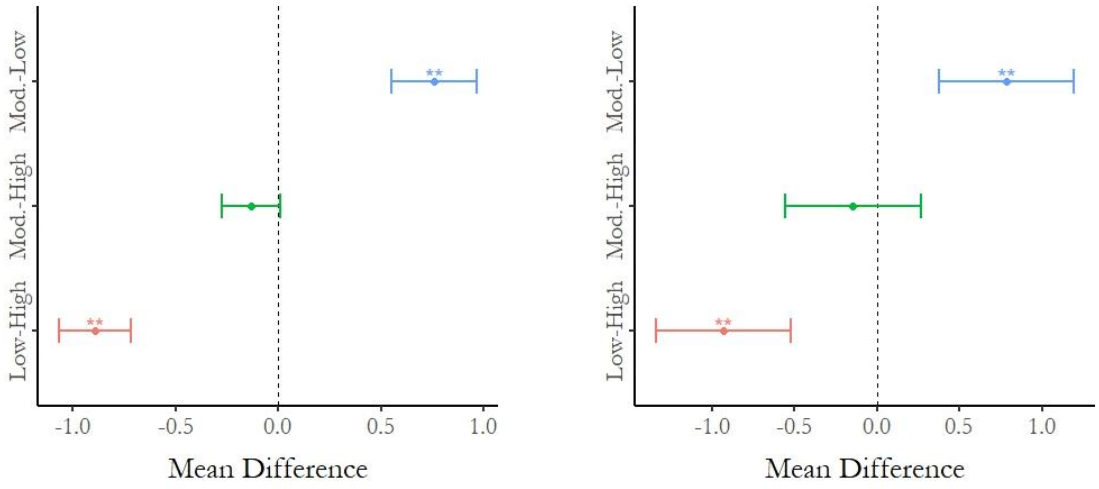

Figure 10. (Top left) distribution of SfM modeled snow for the whole dataset and (top right) the sampled dataset. Group means are indicated by red diamonds. (Bottom left) a Tukey plot of the full dataset and (bottom right) and sampled dataset show the same patterns: modeled snow in low and high severity burn are similar while both moderate and high severity burn are significantly different from low severity burn.

Measured snow depth was compared across classes to see if patterns between measured and modeled snow and burn severity were similar (Figure 10, 11). Like modeled snow depth, measured snow (by mean and median) was lowest in low severity burn, followed by moderate and high severity burn. Also reflected by modeled snow, actual depth in low and high severity burn (adjusted p-value = 0.003) and low and moderate severity burn (p-value = 0.033) was significantly different while snow depth in moderate and high severity burn were not different.

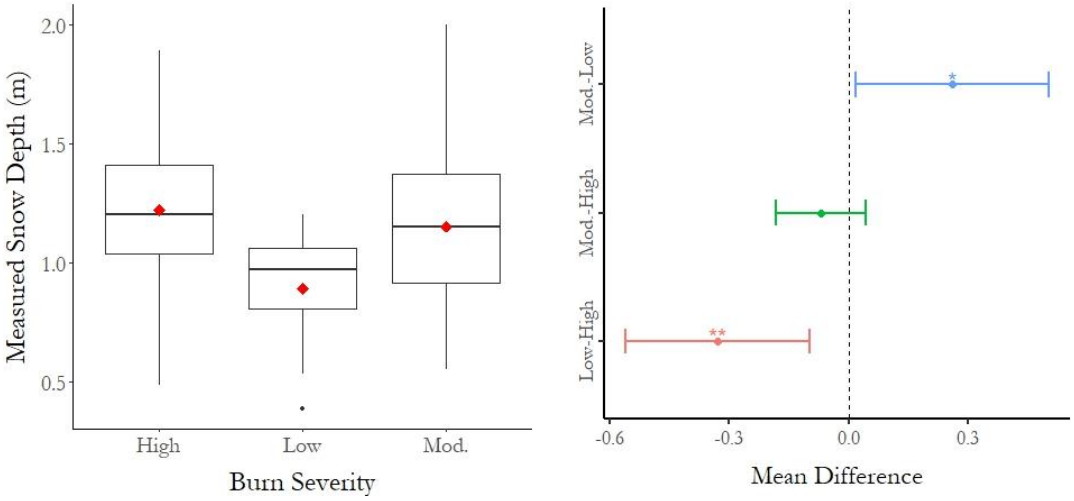

Figure 11. (Left) boxplots showing the distribution of measured snow depth by burn severity class and (right) a Tukey plot that shows measured snow depth is significantly different between low and high severity burn and moderate and low severity burn.

3.2 Snow Covered Area

A confusion matrix comparing February SfM-derived snow extent to coincident Landsat fSCA indicated that 653 modeled snow pixels were correctly classified by the SfM model while 347 pixels were incorrectly classified, such that modeled snow extent was accurate 65% of the time with an error rate of 45% (Table 6, Figure 12). The February SCA model accurately predicted 50% of snow-covered pixels and 81% of snow-free pixels. With a Mcnemar's Test significant p-value (p-value < 10×2^{-16}), we disproved the Mcnemar's Test null hypothesis that the reference and predicted datasets are the same.

A confusion matrix comparing April SfM modeled snow to Landsat fSCA performed more poorly, with 506 modeled snow extent pixels classified correctly while 494 pixels were incorrectly classified, such that modeled snow extent for April was 50% accurate with a 50%

error rate. The April model accurately predicted 38% of snow-free pixels and 76% of snow-covered pixels. A Mcnemar's Test (p-value = 10×5^{-14}) indicated that the April SfM SCA map and Landsat SCA were not equal.

Table 6. Confusion matrices for February (left) and April (right) SfM snow extent and Landsat fSCA, where 'predicted' values are modeled snow extent and 'reference' values are derived from Landsat fSCA. The February snow extent map accurately predicted 65% of all pixels, with 50 and 81% of snow-covered and snow-free pixels correctly predicted, respectively. The April snow extent map accurately predicted 50% of all pixels, with 76 and 38% of snow-covered and snow-free pixels correctly predicted, respectively.

February

	Reference		
Predicted		0	1
	0	430	244
	1	103	223

April

	Reference		
Predicted		0	1
	0	252	79
	1	415	254

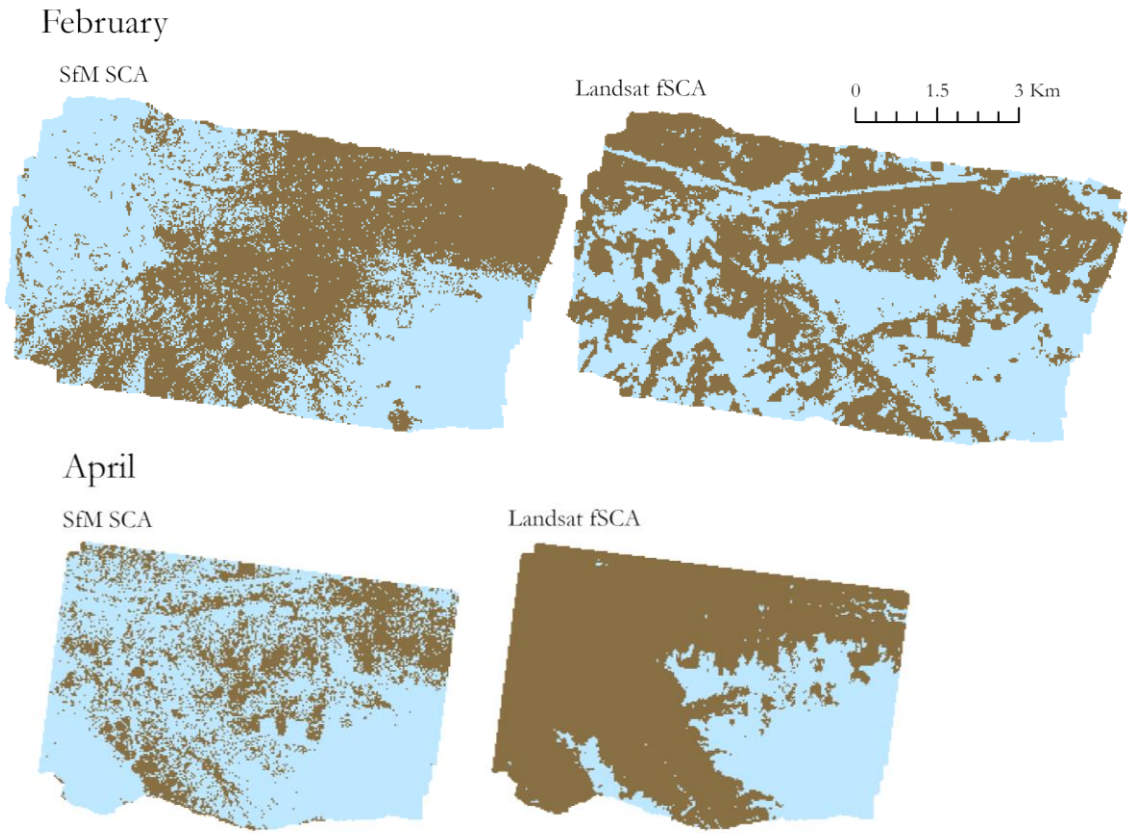

Figure 12. SfM modeled snow extent (left) and LandsatfSCA (right) maps for February (top) and April (bottom). Blue indicates snow-covered pixels and brown indicates snow free pixels. Snow-covered pixels are where canopy adjusted fSCA ≥ 75 and where modeled SCA is greater than 0. All other pixels are snow free.

3.3 Snow Depth Maps

We expected SfM methods to perform best in high severity burn forest. Given that SfM modeled snow in high and moderate severity forests was not statistically different, we constrained snow maps to high and moderate severity burn regions. After constraining February and April snow maps by Landsat fSCA and burn severity and adjusting snow maps by the regression between measured and 0.3-meter resolution modeled snow (found in section 3.1.1), 1000 points were randomly sampled from the constrained domain (April snow depth mean = 1.5 meters, standard deviation = 0.5 meters; February snow depth mean = 2.0 meters, standard deviation = 1.2 meters).

The regression of February modeled snow and driving variables showed RdNBR (p-value =0.002470), elevation (p-value $< 2.2 \times 10^{-16}$), slope (p-value $< 2.2 \times 10^{-16}$), and aspect (p-value varied by aspect) all related significantly to modeled snow depth (February snow depth = -9.8 + 0.00 (RdNBR) + 0.01 (elevation) – 0.33 (slope), adjusted R-squared = 0.53, p-value $< 2.2 \times 10^{-16}$). The same was true for April, where RdNBR (p-value = 0.00), elevation (p-value $< 2.2 \times 10^{-16}$), slope (p-value $< 2.2 \times 10^{-16}$), and aspect (p-value varied by aspect) all related significantly to modeled snow depth (April snow depth = $-4.5 + 2.3 \times 10^{-4}$(RdNBR) + 4.03×10^{-3} (elevation) – 1.2×10^{-2} (slope), adjusted R-squared = 0.58, p-value $< 2.2 \times 10^{-16}$). Aspect was a significant driver of snow and varied positively with snow depth across all directions (aspect p-values varied by direction and were therefore not included in the above model equations).

Similarly to initial regressions, snow depth trended positively with burn severity in February and April. Unlike initial regressions, elevation, slope, and aspect drove variability in ideal snow maps. Snow depth typically increases with elevation due to decreased temperatures and orographic lifting, so the positive relationship between SfM modeled snow and elevation is expected. Snow depth decreases with increased vegetation cover due to canopy interception and long-wave radiative forcing. While we did not expect to see this relationship in the model as vegetation density drives error in SfM modeling, we expected to see correlations between vegetation and modeled snow depth estimates. However, vegetation variables were not significantly related to modeled snow depth.

Snow depth maps constrained to snow-covered, high and moderate severity burn regions showed huge increased in snow depth in the southeast quadrant (Figure 13). It is difficult to determine if this is a snow signal or elevation signal, especially as snow increases with elevation. As snow depth appears to increase with distance from GCPs, this may also be influencing depth maps. A final possibility is that error increases towards the edge of the survey region.

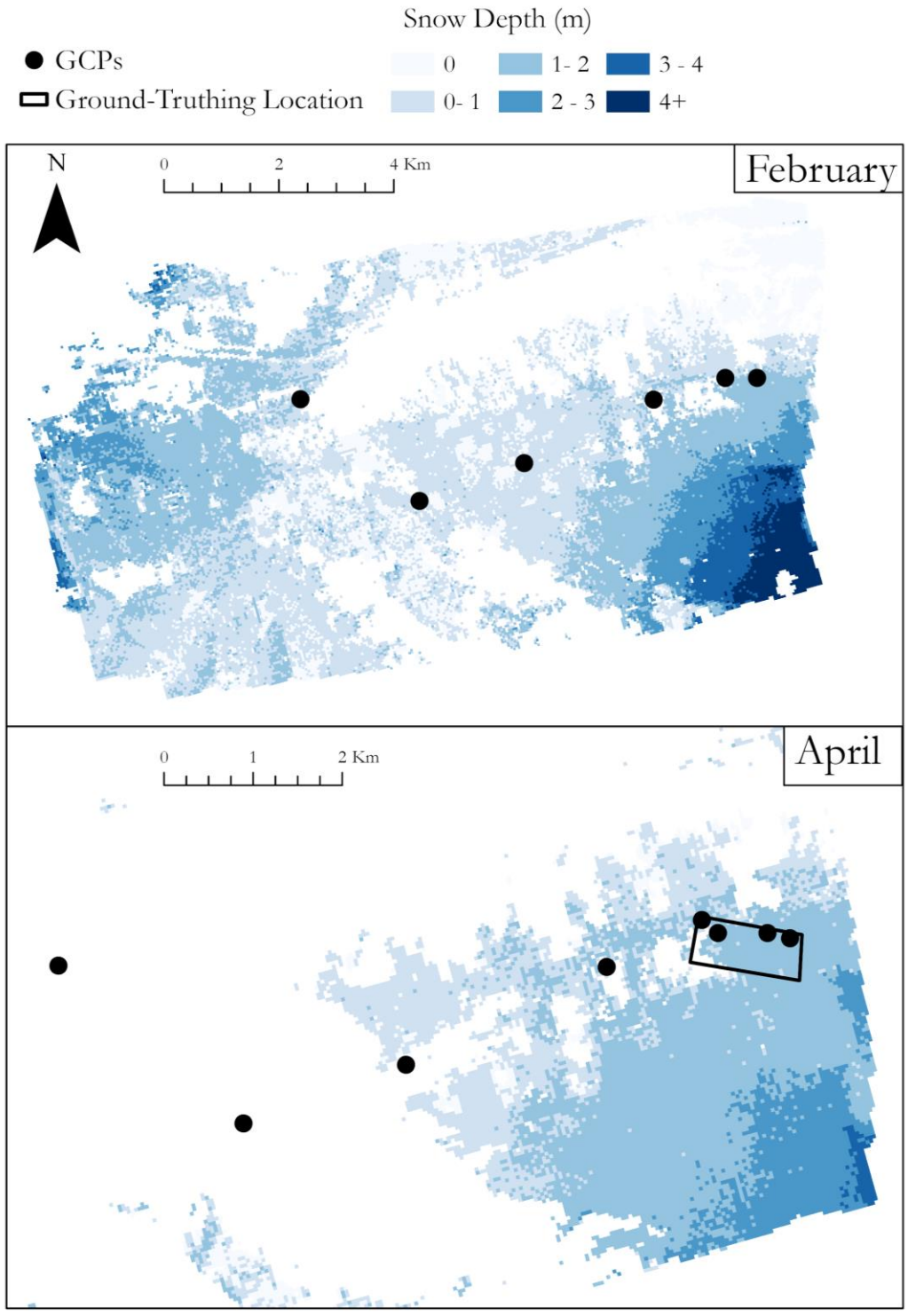

Figure 13. Snow depth maps constrained to high and moderate severity burn, snow covered regions for February (top) and April (bottom). Ground control points deployed in each survey are included.

3.4 A Qualitative Assessment of Point-Cloud Confidence

When estimating locations of points in a dense cloud, *Metashape* produces a confidence value for every point, where confidence is based upon the number of depth maps used to construct a scene. Depth maps are 2-D images that convey the distance from a pixel to a camera. As can be seen in Figure 14 (where red indicates low point confidence and blue indicates high point confidence), open regions have high point confidence. Three logged regions near the center of the map exhibit the greatest density of high confidence (blue) points of the entire point cloud. By contrast, forested regions north of the logged regions and in the SW corner of the dense clouds appear to have the lowest confidence values. High severity burn regions, visible to the immediate NW and SE of the logged regions, have point confidence values that lie between forest and open region point confidence.

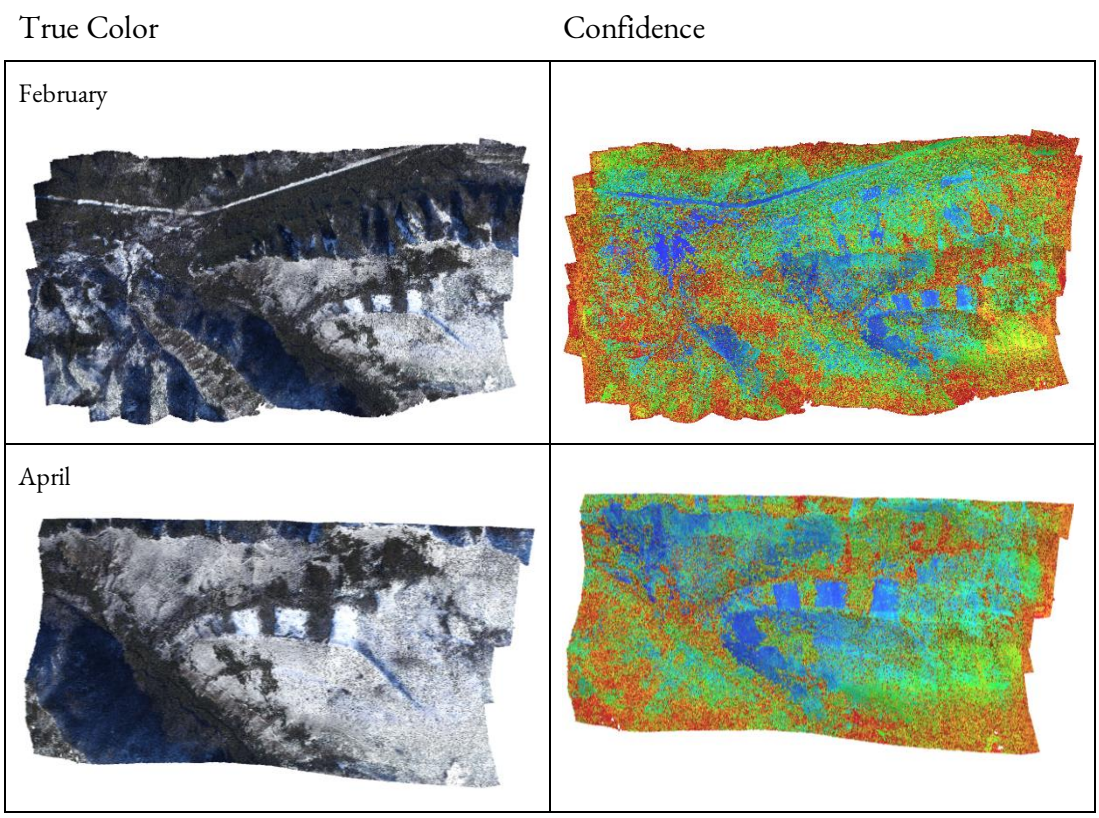

Figure 14. True color point clouds (left) and confidence-colored (right) point clouds from each survey, where blue indicates high confidence and red indicates low confidence. Areas of low vegetation correlate with high point confidence (blue) where densely forested and shaded regions correlate with low point cloud confidence (red). Interestingly, high severity burned regions, such as the southeast quadrant, appear to indicate improved point cloud confidence compared to forested regions. This is most apparent in the April point cloud.

Discussion

Structure-from-motion is a valuable remote sensing technique that enables snow hydrologists to survey snow at a low cost and with minimal equipment compared to LiDAR (Westoby et al. 2012; Bühler et al. 2015). In recent years, SfM has been used to survey snowy regions up to 300 km^2 with centimeter accuracy and meter resolution (Buhler et al. 2016, Meyer and Skiles 2019). Trees in these surveys were either masked or else low enough in height or density as to minimally affect snow-mapping.

Knowing that SfM is an optical sensing method and is therefore typically employed in non-forested environments where the ground is clearly visible, we investigated the potential of this method to survey snow in burned forests where canopy cover is greatly reduced. With the proliferation of fire in the West and the influence of burned forest on snow processes, downstream water resources, and hazards risk, a rapidly deployable and financially accessible method of surveying snow is particularly valuable in burned regions. While trees inevitably impact the quality of snow maps, we asked: can we detect a snow signal in burned forests at the basin scale with airborne SfM, and if so, what is the strength of that signal? To answer these questions, we must disentangle a snow signal from the trees. This is a challenging task as factors that drive error, broadly vegetation, burn severity, and topography, also influence error in SfM mapping.

4.1 Modeled and Measured Snow Regressions

We saw that at 0.3-meter resolution, there was an 18% correlation between measured snow depth and SfM modeled depth. Though this correlation is weak, it indicated that we may be sensing snow depth through the trees. This correlation decreased to 13% when modeled snow depth was smoothed to 30-meters. While this could be random, it may also indicate that a high-resolution was critical to sensing gaps between trees, while DEM smoothing aggregated 'noise' from trees. In both 0.3- and 30-meter resolution regressions, the adjusted R-squared indicated significant relationships between measured and modeled snow. Because of this, we used the relationship between measured and modeled snow to adjust sampled SfM snow depth values and maps.

4.2 Variability in Modeled Snow by Classified and Continuous Burn Severity

It is clear we were not able to detect absolute snow depth in these surveys. Still, we can assert that SfM models estimated snow in high and moderate severity burn forests in a way that was distinct from low severity burned forests. This result is clearly represented by our ANOVA comparing modeled snow by burn severity classifications (i.e., figure 11). Here, even when controlling for disparate sample size, we see much greater variability in modeled snow in low severity burn than in high and moderate severity burn.

Some snow depth values in low severity burn regions were negative. When Meyers and Skiles (2019) surveyed a 300 km^2 region, vegetation-classified pixels produced negative values

ranging from -4 to -28 m. This may be caused by slight lateral offsets between differenced models that feature large spikes in 'elevation' where trees were not resolved by point cloud classification, or this could be caused by limitations of *Metashape* to resolve terrain elevation in forests altogether. Interestingly, in both measured and modeled snow depth, the mean and median were greatest in high severity burn, followed by moderate and lastly low severity burn. While we cannot assert with our data if this is due to SfM snow depth maps accurately capturing variability in the depth of imaged snow, this result is compelling and warrants further investigation.

4.3 Snow Covered Area and Snow Depth Maps

We found that SfM snow maps were not statistically related to Landsat fSCA snow extent maps. February SfM modeled snow extent correctly predicted pixels 65% of the time where April SfM modeled snow extent accurately predicated only 50% of pixels. However, a visual assessment of SfM snow cover maps indicated that the most disagreement with Landsat fSCA maps occurred in low and unburned forest where snow cover is least visible. These findings warrant repeating this analysis in high and moderate burn severity regions only.

We saw modeled snow in the ideal modeling region "behave" in expected ways. Primarily, snow depth increased with elevation and burn severity. We expected modeled snow to correlate with vegetation density as vegetation drives error in SfM models, but vegetation was not a significant driver of variability in SfM snow maps in February or April.

Drivers of variability in snow-depth maps were different between initial regressions and regressions in ideal mapping regions. There are several explanations for this. After constraining the study region to high severity burn and snow-covered regions, the influence of topographic variables on SfM-derived snow depth map become statistically significant and/or drivers of variability may change depending on the sampling area. Sampling for snow depth modeling was derived from a 6 km^2 region whereas ground-truthed points used for error modeling were sampled from a 0.32 km^2 region. It is possible that topographic relief is amplified at higher elevations where there is greater surface detail. The final possibility is that distortions in the bare earth DEM influenced results of basin-scale (snow extent and ideal snow map) analyses.

4.4 Distortions in the Bare-Earth Map

Snow depth maps constrained to snow-covered, high and moderate severity burn regions showed huge increases in estimated depth in the SE corner of the map. We delved further into this observation by subtracting a LiDAR-derived DEM from our bare-earth map (the same LiDAR DEM from which elevation, slope, and aspect data was derived) (Figure 15). It is important to note that LiDAR can be used to create terrain models (maps without surface features like trees) in densely vegetated regions much more effectively than SfM is able to. This is why highly vegetated regions in Figure 15 (purple regions that are 7+ meters) are clearly visible in the DEM of difference. It should also be noted that there is likely an offset between the LiDAR DEM and the SfM bare-earth DEM. As we were concerned with only variability in the

DEM of difference, we did not calculate an offset (though from randomly sampling points along roads, regions we expect to see no change, there appears to be an offset of about 25 meters).

Figure 15 indeed shows that the difference between the SfM bare-earth map is greatest in the southeast corner, where the SfM map is greater than LiDAR. The magnitude of the difference between LiDAR and the SfM map in this region indicates that there is likely distortion in the bare-earth model. Given that GCPs were roughly colinear, it is possible that there is a rotation in the bare-earth DEM around the axis of the GCPs. This distortion likely impacted snow extent maps and ideal snow depth maps, as these analyses were completed at the basin scale. Regressions between measured and modeled snow, initial multilinear regressions, and ANOVAs of modeled snow across burn severity were completed with point data in the ground-measurement survey region. This survey region was small (0.3 km^2) and in-line with ground control. Because of this, we expect these results to be unaffected by DEM rotation around the axis of GCPs. Distortion in the bare-earth DEM must be corrected and basin-scale analyses repeated to achieve reliable results.

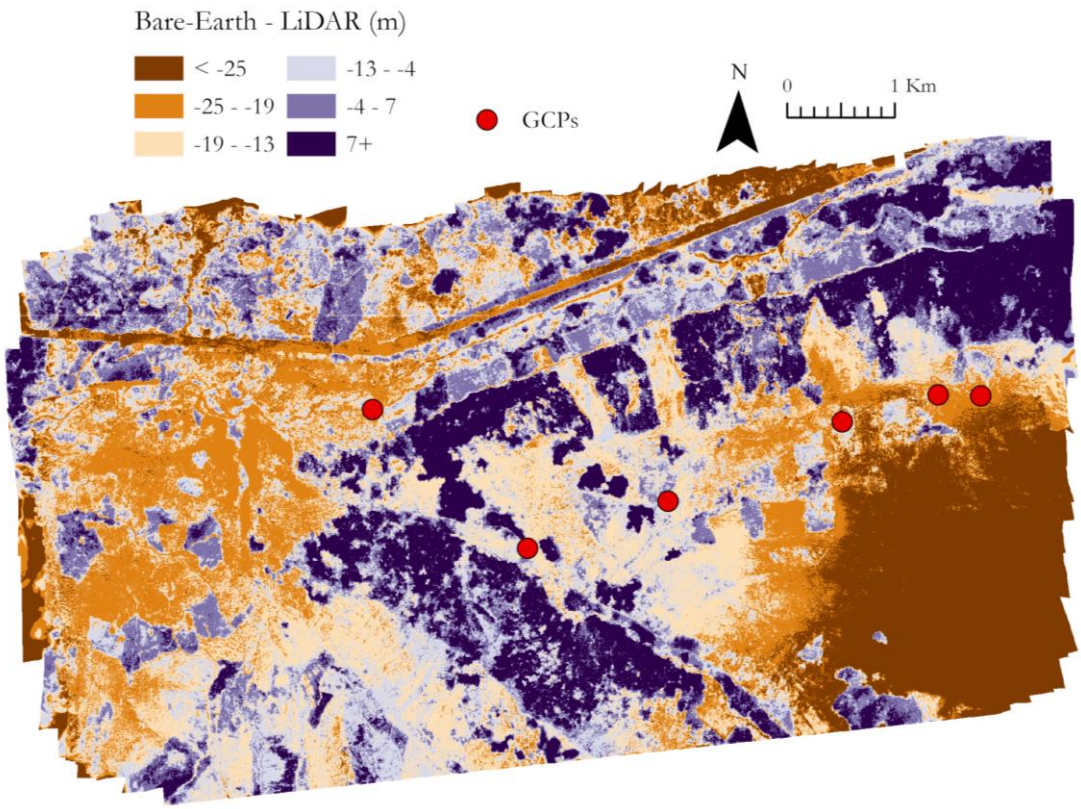

Figure 15. LiDAR data subtracted from a DEM derived from the bare-earth flight. An offset between LiDAR and the BE flight has not been applied (we expect this offset to be about 23 meters). As expected, the SfM BE map indicates greater elevation in forested regions. The southeast corner of the map shows the greatest difference between LiDAR and the SfM map. This is likely due to distortions in the SfM BE map.

4.4. Lessons Learned and Study Recommendations

We flew an airplane over a 27 and 15 km^2, densely forested burn scar. These surveys were highly experimental and novel, and produced interesting results that suggest high severity burned forest may be a more suitable location for SfM at the basin scale than unburned forests. Throughout the course of this study, we learned that more thorough georeferencing could majorly improve point cloud location estimates. More thorough georeferencing could look like a higher accuracy GPS with flight orientation parameters included or more dispersed and a greater quantity of GCPs. Greater dispersal of GCPs would likely resolve the rotation issues we

encountered in basin-scale maps. Given the remote location and size of our study region, improving GPS accuracy is more ideal than introducing more GCPs. We also learned that other point cloud classification software is often used in tandem with *Metashape* to produce a final point cloud. Based off these lessons, we offer these recommendations:

(1) Post-processing the navigation file output from the Waldo Flight Control Software that contains high-resolution flight location and orientation data could majorly improve image position estimates. The GPS in the WaldoAir (the OEMStar from NovAtel, a single-frequency multi-constellation GNSS receiver) has 1.5-meter accuracy without post-processing, which is the accuracy of the coordinates embedded in photo EXIF files. Additionally, the GPS was placed on the dashboard of the plane during flights, and no offset was calculated between the sensor and the GPS (this offset was roughly 1 meter). Increasing image geotag accuracy through incorporating flight orientation parameters and post-processing while securing the GPS to a position with a known distance from the WaldoAir sensors may improve model outputs without the need for additional GCPs. Nolan et al. (2015) used GCPs only to test SfM model performance (rather than for georeferencing) and were able to survey snow with centimeter to decimeter accuracy, but they employed a multi-frequency GPS with 10 cm accuracy and a calculated and consistent offset from the sensor.

(2) More rigorous point cloud classification and filtering. For simplicity's sake, we classified our point cloud in *Metashape*. While *Metashape* classification was essential for digital terrain models, it was clear through a visual inspection of the point cloud that some of trees, particularly in high severity burned regions, were not correctly classified. This was apparent as no points were classified as high vegetation in regions of stand-replacing fire. As noted by Meyer and Skiles (2019), Point Cloud Library, LAStools, and Point Data Abstraction Library are popular point-cloud processing software. Adequately filtering a point cloud in high severity burn is essential to creating a digital terrain model representative of the snow surface.

Conclusion

We expected that variability would be greatest in unburned forests and smallest in high severity burned forests with low vegetation density. Initial regressions showed us that variability in SfM-derived snow depth was driven by burn severity (RdNBR) at 0.3- and 30-meter resolutions. Modeled snow increased with burn severity, a relationship we expect to see in snow in burned forests. While we cannot validate that this pattern was due to a snow signal in our snow depth models, the differences in variability and magnitude of modeled snow in low versus moderate and high severity burn was striking, and we can assert that SfM modeling in low severity burn regions was much more variable than in moderate and high severity burn regions. In this way, our results suggest SfM surveying may be useful in moderate and high severity burn regions.

Despite issues with the bare-earth map, our findings still suggest that SfM-derived snow depth mapping at the basin scale may be more accurate in burned forests than unburned forests, but more work is needed. We observed variability in high severity burned forest to be distinct and more predictable than error in low and moderate severity burn. Given the influence that burned forests exerts on snow, downstream water resource, and hazards risk, and the affordability of SfM when surveying snow at large spatial scales compared techniques like LiDAR, this work indicates that research into SfM surveys of burned basins stands to benefit watershed managers and snow hydrologists alike.

References

Abatzoglou, John T., David E. Rupp, Larry W. O'Neill, and Mojtaba Sadegh. 2021. "Compound Extremes Drive the Western Oregon Wildfires of September 2020." *Geophysical Research Letters* 48 (8). https://doi.org/10.1029/2021gl092520.

Adams, Marc S. 2016. "Mapping Snow Depth in Alpine Terrain with Unmanned Aerial Systems (UASs): Potential and Limitations." *The Cryosphere; Katlenburg-Lindau* 10 (3): 1075–88.

Adams, Marc S., Yves Bühler, and Reinhard Fromm. 2018. "Multitemporal Accuracy and Precision Assessment of Unmanned Aerial System Photogrammetry for Slope-Scale Snow Depth Maps in Alpine Terrain." *Pure & Applied Geophysics; Basel* 175 (9): 3303–24.

Adrian Harpold,Paul Brooks,Seshadri Rajagopal,Ingo Heidbuchel,Angela Jardine,and Clare Stielstra. 2012. "Changes in Snowpack Accumulation and Ablation in the Intermountain West." *WATER RESOURCES RESEARCH*, February. https://doi.org/10.1029/2012WR011949.

Barnett, T. P., J. C. Adam, and D. P. Lettenmaier. 2005. "Potential Impacts of a Warming Climate on Water Availability in Snow-Dominated Regions." *Nature* 438 (7066): 303–9.

Barnhart, Theodore B., Noah P. Molotch, Ben Livneh, Adrian A. Harpold, John F. Knowles, and Dominik Schneider. 2016. "Snowmelt Rate Dictates Streamflow." *Geophysical Research Letters* 43 (15): 8006–16.

Bühler, Y., M. Marty, L. Egli, J. Veitinger, T. Jonas, P. Thee, and C. Ginzler. 2015. "Snow Depth Mapping in High-Alpine Catchments Using Digital Photogrammetry." *The Cryosphere* 9 (1): 229–43.

Carrivick, Jonathan L., Mark W. Smith, and Duncan J. Quincey. 2016. *Structure from Motion in the Geosciences*. Wiley & Sons, Limited, John.

Clow, David W. 2010. "Changes in the Timing of Snowmelt and Streamflow in Colorado: A Response to Recent Warming." *Journal of Climate* 23 (9): 2293–2306.

Daniel Viviroli, Hans H. Durr, Bruno Messerli, Michel Meybeck, and Rolf Weingartner. n.d. "Mountains of the World, Water Towers for Humanity: Typology, Mapping, and Global Significance." https://doi.org/10.1029/2006WR005653.

DeWalle, David R., and Albert Rango. 2008. *Principles of Snow Hydrology*. Cambridge University Press.

Gleason, Kelly E., Joseph R. McConnell, Monica M. Arienzo, Nathan Chellman, and Wendy M. Calvin. 2019. "Four-Fold Increase in Solar Forcing on Snow in Western U.S. Burned Forests since 1999." *Nature Communications* 10 (1): 2026.

Gleason, Kelly E., Anne W. Nolin, and Travis R. Roth. 2013. "Charred Forests Increase Snowmelt: Effects of Burned Woody Debris and Incoming Solar Radiation on Snow Ablation." *Geophysical Research Letters* 40 (17): 4654–61.

Knowles, John F., Noah P. Molotch, Ernesto Trujillo, and Marcy E. Litvak. 2018. "Snowmelt-driven Trade-offs between Early and Late Season Productivity Negatively Impact Forest Carbon Uptake during Drought." *Geophysical Research Letters* 45 (7): 3087–96.

Knowles, Noah, Michael D. Dettinger, and Daniel R. Cayan. 2006. "Trends in Snowfall versus Rainfall in the Western United States." *Journal of Climate* 19 (18): 4545–59.

Li, Dongyue, Melissa L. Wrzesien, Michael Durand, Jennifer Adam, and Dennis P. Lettenmaier. 2017. "How Much Runoff Originates as Snow in the Western United States, and How Will That Change in the Future?" *Geophysical Research Letters* 44 (12): 6163–72.

McCabe, Gregory J., Martyn P. Clark, and Lauren E. Hay. 2007. "Rain-on-Snow Events in the Western United States." *Bulletin of the American Meteorological Society* 88 (3): 319–28.

Meyer, Joachim, Jeffrey S. Deems, Kat J. Bormann, David E. Shean, and S. Mckenzie Skiles. 2022. "Mapping Snow Depth and Volume at the Alpine Watershed Scale from Aerial Imagery Using Structure from Motion." *Frontiers of Earth Science in China* 10. https://doi.org/10.3389/feart.2022.989792.

Meyer, Joachim, and S. Mckenzie Skiles. 2019. "Assessing the Ability of Structure from Motion to Map High-resolution Snow Surface Elevations in Complex Terrain: A Case Study from Senator Beck Basin, CO." *Water Resources Research* 55 (8): 6596–6605.

Mote, Philip W. 2003. "Trends in Snow Water Equivalent in the Pacific Northwest and Their Climatic Causes." *Geophysical Research Letters* 30 (12). https://doi.org/10.1029/2003gl017258.

Mote, Philip W., Alan F. Hamlet, Martyn P. Clark, and Dennis P. Lettenmaier. 2005. "DECLINING MOUNTAIN SNOWPACK IN WESTERN NORTH AMERICA*." *Bulletin of the American Meteorological Society* 86 (1): 39–50.

Mote, Philip W., Li Sihan, Dennis P. Lettenmaier, Mu Xiao, and Ruth Engel. 2018. "Dramatic Declines in Snowpack in the Western US." *NPJ Climate and Atmospheric Science; London* 1 (1): s41612–018.

Musselman, Keith N., Nans Addor, Julie A. Vano, and Noah P. Molotch. 2021. "Winter Melt Trends Portend Widespread Declines in Snow Water Resources." *Nature Climate Change* 2021 (April). https://doi.org/10.1038/s41558-021-01014-9.

Musselman, Keith N., Martyn P. Clark, Changhai Liu, Kyoko Ikeda, and Roy Rasmussen. 2017. "Slower Snowmelt in a Warmer World." *Nature Climate Change* 7 (3): 214–19.

Musselman, Keith N., Flavio Lehner, Kyoko Ikeda, Martyn P. Clark, Andreas F. Prein, Changhai Liu, Mike Barlage, and Roy Rasmussen. 2018. "Projected Increases and Shifts in Rain-on-Snow Flood Risk over Western North America." *Nature Climate Change* 8 (9): 808–12.

Nolan, M., C. Larsen, and M. Sturm. 2015. "Mapping Snow Depth from Manned Aircraft on Landscape Scales at Centimeter Resolution Using Structure-from-Motion Photogrammetry." *The Cryosphere* 9 (4): 1445–63.

Nolin, Anne W., and Christopher Daly. 2006a. "Mapping 'At Risk' Snow in the Pacific Northwest." *Journal of Hydrometeorology* 7 (5): 1164–71.

Over, Jin-Si R., Andrew C. Ritchie, Christine J. Kranenburg, Jenna A. Brown, Daniel D. Buscombe, Tom Noble, Christopher R. Sherwood, Jonathan A. Warrick, and Phillipe A. Wernette. 2021. "Processing Coastal Imagery with Agisoft Metashape Professional Edition, Version 1.6—Structure from Motion Workflow Documentation." 2021-1039. U.S. Geological Survey. https://doi.org/10.3133/ofr20211039.

Steltzer, Heidi, Chris Landry, Thomas H. Painter, Justin Anderson, and Edward Ayres. 2009. "Biological Consequences of Earlier Snowmelt from Desert Dust Deposition in Alpine Landscapes." *Proceedings of the National Academy of Sciences of the United States of America* 106 (28): 11629–34.

Stewart, Iris T., Daniel R. Cayan, and Michael D. Dettinger. 2004. "Changes in Snowmelt Runoff Timing in Western North America under a `Business as Usual' Climate Change Scenario." *Climatic Change* 62 (1): 217–32.

Sturm, Matthew, Michael A. Goldstein, and Charles Parr. 2017. "Water and Life from Snow: A Trillion Dollar Science Question." *Water Resources Research* 53 (5): 3534–44.

Trujillo, Ernesto, and Noah P. Molotch. 2014. "Snowpack Regimes of the Western United States." *Water Resources Research* 50 (7): 5611–23.

Trujillo, Ernesto, Noah P. Molotch, Michael L. Goulden, Anne E. Kelly, and Roger C. Bales. 2012. "Elevation-Dependent Influence of Snow Accumulation on Forest Greening." *Nature Geoscience* 5 (10): 705–9.

Walker, Branden, Evan J. Wilcox, and Philip Marsh. 2021. "Accuracy Assessment of Late Winter Snow Depth Mapping for Tundra Environments Using Structure-from-Motion Photogrammetry." *Arctic Science* 7 (3): 588–604.

Westerling, A. L., H. G. Hidalgo, D. R. Cayan, and T. W. Swetnam. 2006. "Warming and Earlier Spring Increase Western U.S. Forest Wildfire Activity." *Science* 313 (5789): 940–43.

Westoby, M. J., J. Brasington, N. F. Glasser, M. J. Hambrey, and J. M. Reynolds. 2012a. "'Structure-from-Motion' Photogrammetry: A Low-Cost, Effective Tool for Geoscience Applications." *Geomorphology* 179 (December): 300–314.

Winchell, Taylor S., David M. Barnard, Russell K. Monson, Sean P. Burns, and Noah P. Molotch. 2016. "Earlier Snowmelt Reduces Atmospheric Carbon Uptake in Midlatitude Subalpine Forests." *Geophysical Research Letters* 43 (15): 8160–68.

Appendix A: *Agisoft Metashape* Mapping Specifications and Camera Calibration Parameters

Table 7. Summary information of snow-on and bare-earth products following bundle adjustment. As the bare-earth flight was re-processed with each snow-on flight, the unique bare-earth raster for each snow-on flight is denoted "BE snow-on survey date".

Flight	Images	Tie Points	Projections	Ground Res.	Reprojection Error	Export Res. (m/pix)
BE April 28	1,154	1,096,694	2,522,988	13.2 cm/pix	0.284 pix	0.3
April 28	1,017	1,461,913	3,467,547	11.5 cm/pix	0.269 pix	0.3
BE Feb. 25	1,154	1,685,268	3,570,701	13.2 cm/pix	0.262 pix	0.3
February 25	1,146	2,272,591	5,294,181	11.6 cm/pix	0.273	0.3

Table 8. Camera specifications including camera model, resolution, focal length, pixel size, and calibration. These parameters were the same for both cameras so are only detailed once. These parameters were the same for all flights.

Camera Model	Resolution	Focal Length	Pixel Size	Precalibrated
Canon EOS 5DS R	8688 x 7592	50 mm	4.24 x 4.24 μm	No

Table 9. Camera (image) Error Estimates.

Flight	X error (m)	Y error (m)	Z error (m)	XY error (m)	Total Error (m)
BE February 25	NA	NA	NA	NA	NA
February 25	68.9	10.7	7.4	69.7	70.1
BE April 28	52.7	9.8	8.0	53.6	54.2
April 28	65.4	33.4	7.2	73.4	73.7

Table 10. Ground Control Point Error Estimates.

Flight	X error (m)	Y error (m)	Z error (m)	XY error (m)	Total Error (m)
BE February 25	NA	NA	NA	NA	NA
February 25	1.0	1.1	0.8	1.5	1.7
BE April 28	1.0	0.5	0.3	1.1	1.2
April 28	0.4	0.5	1,1	0.6	1.3

Appendix B: Survey Digital Elevation Models and Orthomosaics

A. Bare-Earth Flight

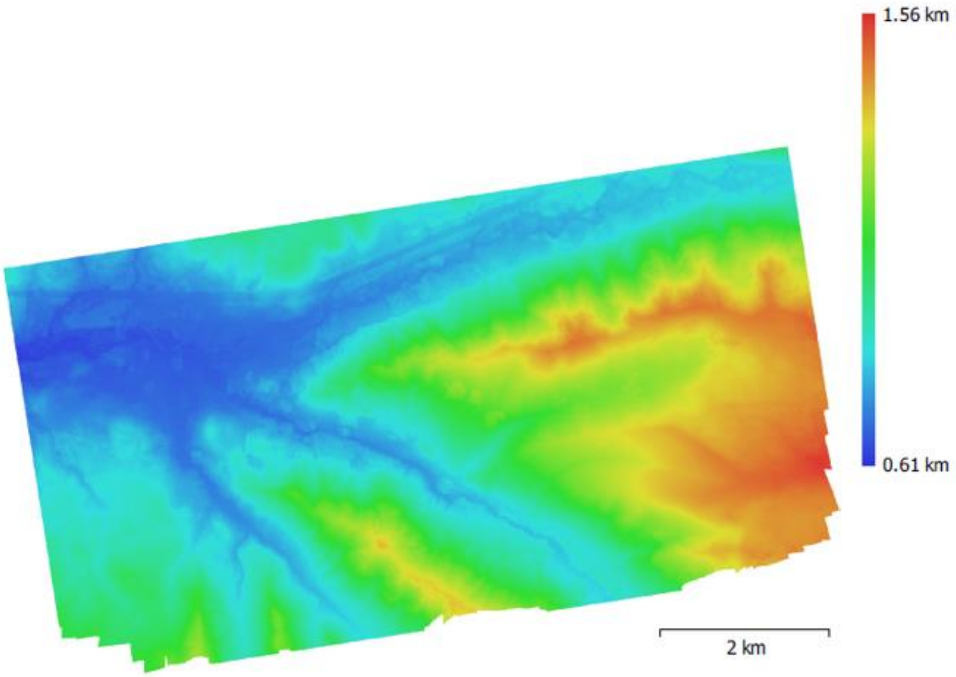

Figure 16. A DEM of the bare-earth flight.

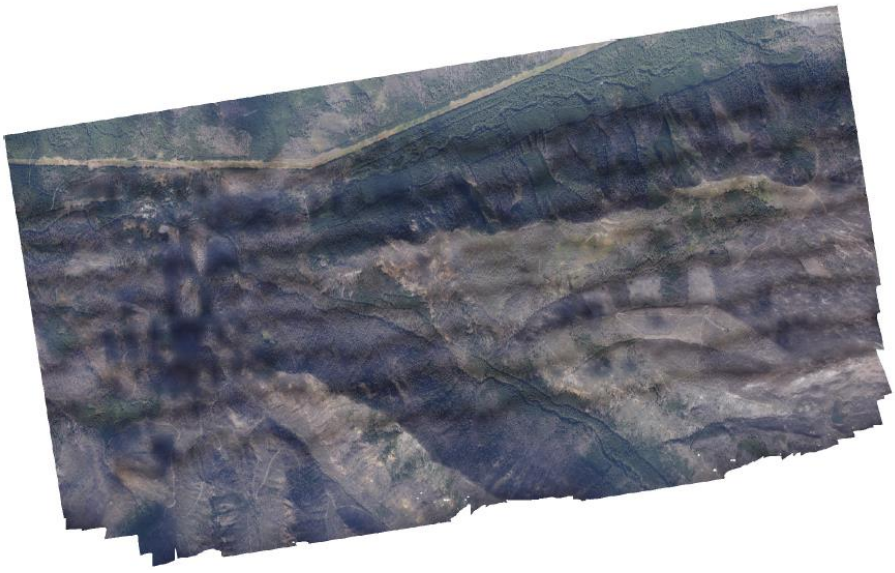

Figure 17. An orthomosaic of the bare-earth flight.

B. February Flight

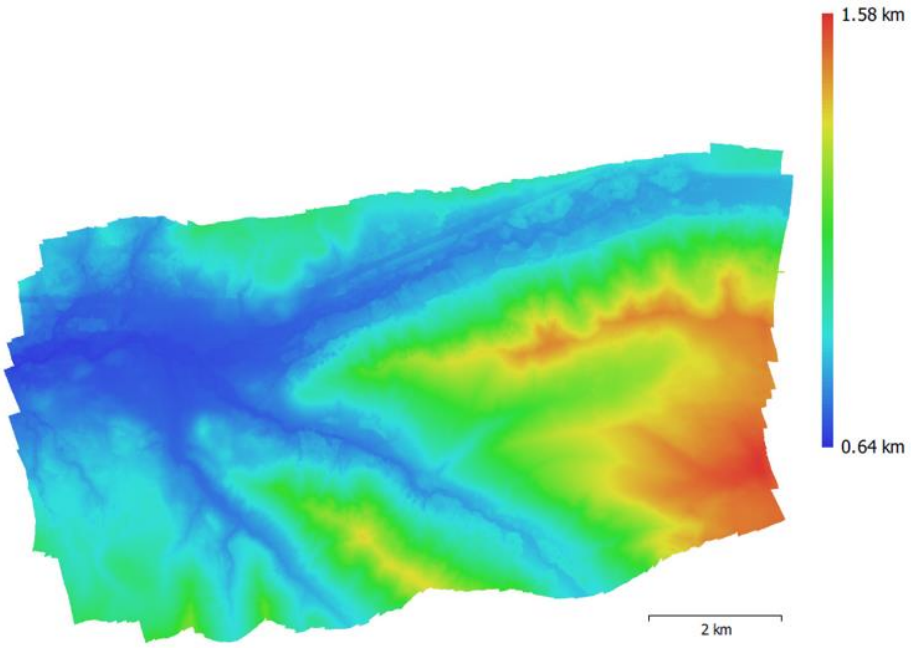

Figure 18. A DEM of the February 25th flight.

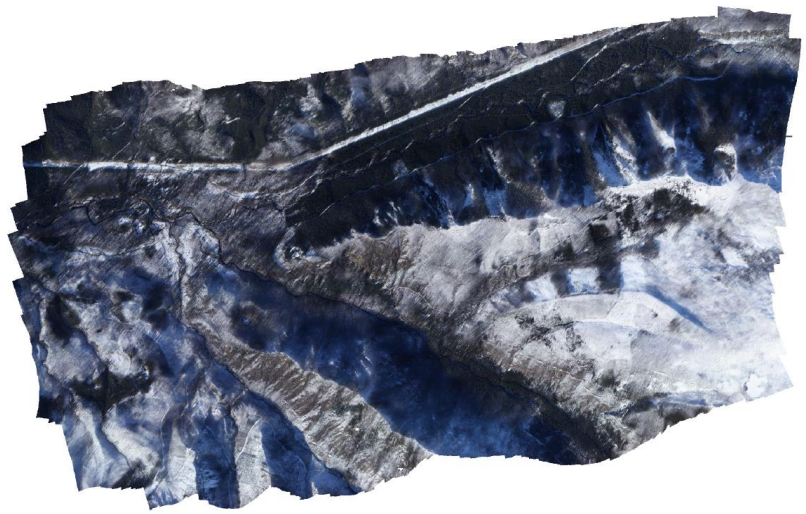

Figure 19. An orthomosaic of the February 25th flight.

C. April Flight

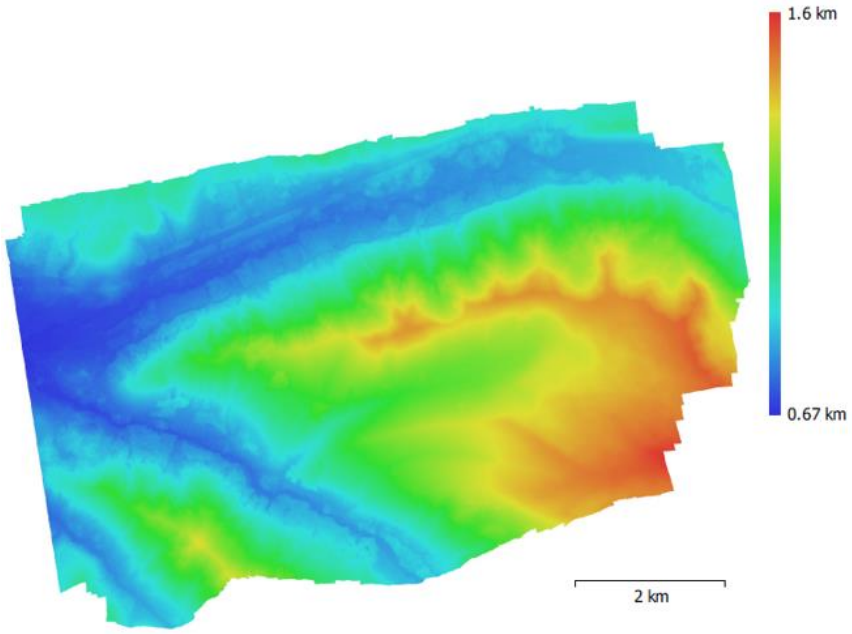

Figure 20. A DEM of the April 28th flight.

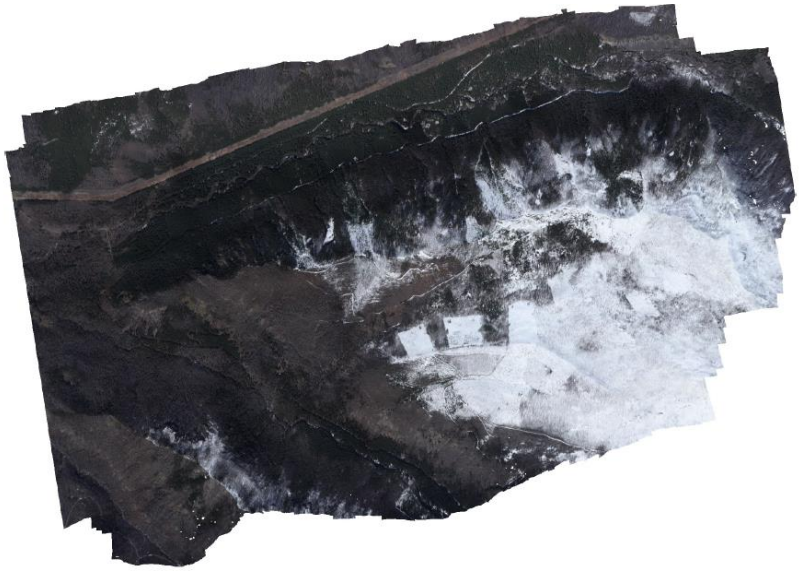

Figure 21. An orthomosaic of the April 28th flight.